remote sensing

MDPI

Article

Effects of the Gully Land Consolidation Project on Geohazards on a Typical Watershed on the Loess Plateau of China

Xiaochen Wang [1], Qiang Xu [1,*], Chuanhao Pu [1], Weile Li [1], Kuanyao Zhao [2], Zhigang Li [1], Wanlin Chen [1] and Dehao Xiu [1]

[1] State Key Laboratory of Geohazard Prevention and Geoenvironment Protection, Chengdu University of Technology, Chengdu 610059, China
[2] College of Architecture and Civil Engineering, Huanghuai University, Zhumadian 463000, China
* Correspondence: xq@cdut.edu.cn

Abstract: From 2011 to 2013, a mega project, known as the Gully Land Consolidation Project (GLCP), was implemented in the hilly gully region atop China's Loess Plateau. However, the GLCP involved large-scale slope excavation and gully backfilling that changed the local geological environment, which led to serious geohazards, such as erosion, soil salinization, and dam failure. In this study, various geohazards caused by the GLCP in the Gutun watershed (GTW) were investigated by combined remote sensing analysis, geophysical exploration, and field surveys, and the relationships between the hazards were also explored. According to the achieved results, increased soil erosion with an average doubling from 2018 to 2020 is widely distributed in the GTW. Furthermore, 195 areas containing clear evidence of salt precipitates were observed in some of the newly created arable lands, especially downstream of the dam. This was mainly attributed to the high water table, evaporation, and soluble salt concentration of the loess. Fifty-nine newly built silt dams, primarily located in the branch channels and at the gully mouth of the Gutun channel, broke in 2020. The osmotic damage and softening caused by the combined effect of the incomplete compaction of the dam body and concentrated heavy rainfall were the main reasons of the dam breaks. The different types of disasters in the GTW after the implementation of the GLCP show a strong spatial relationship that follows the surface water flow path and forms a disaster chain consisting of slope erosion, silt dam breaks, and the soil salinization of near-dam farmlands downstream. This disaster chain amplifies disaster risks and losses. These findings can guide the improvement of the GLCP and inform geohazard mitigation strategies in areas impacted by the GLCP.

Keywords: loess plateau; gully land consolidation project; postconstruction geohazards; disaster chains

Citation: Wang, X.; Xu, Q.; Pu, C.; Li, W.; Zhao, K.; Li, Z.; Chen, W.; Xiu, D. Effects of the Gully Land Consolidation Project on Geohazards on a Typical Watershed on the Loess Plateau of China. *Remote Sens.* **2023**, *15*, 113. https://doi.org/10.3390/rs15010113

Academic Editors: Yi Wang, Jun Hu and Norman Kerle

Received: 4 October 2022
Revised: 16 December 2022
Accepted: 17 December 2022
Published: 25 December 2022

1. Introduction

The Loess Plateau in northwestern China encompasses approximately 6.6% of China's land area and is an important producer of food in China [1]. However, the Loess Plateau is undergoing severe soil erosion, and gullies are frequently developing as a result. This has led to the frequent occurrence of natural disasters in the fragile ecological environment of the Loess Plateau [2]. In addition, soil erosion has also led to the shrinking of flat loess tablelands and the increased scarcity of land resources, which severely restricts local agricultural development [3,4]. Additionally, as society develops and the number of people rapidly increases, the area available for cultivation and for people to build houses is becoming increasingly scarce [5]. As a result, the land resource scarcity problem has intensified the conflict between humanity and nature on the Loess Plateau. Thus, the habitat and environment have further deteriorated, and local people are faced with serious problems such as the scarcity of arable land and limited economic development [6].

The "Grain for Green Project" was launched by the Chinese government in 2000 to alleviate soil erosion on the Loess Plateau [7,8]. Over the 20 years that have passed

since the project was implemented, the ecological environment of the Loess Plateau has been greatly improved, and the vegetation cover has nearly doubled [9–11]. However, large-scale reforestation has led to a large reduction in arable land on the Loess Plateau, which substantially affects the production and livelihood of local residents (Figure 1a) [12]. Recently, the Gully Land Consolidation Project (GLCP) was implemented by the local government in loess gully areas to alleviate these problems and compensate for the loss of arable land [6,13–15]. The GLCP is a new type of gully land management approach that integrates dam construction, wasteland management, and ecological construction [16]. Specifically, the focus of the GLCP is to fill gullies by cutting slopes at the foothills in various small watershed units [12], thereby leveling and expanding arable land to create large areas of new agricultural land [17] (Figure 1b). Additionally, related hydraulic projects, such as dams and reservoirs, were built along the water systems within the watershed to prevent the flooding of agricultural land and intercept sediments (Figure 1c). Vegetation was planted along the excavated slopes to provide erosion control (Figure 1d). In principle, the GLCP conducts reforestation on hillsides while creating new farmland in gullies through land consolidation [18]. It is undeniable that the GLCP has alleviated the shortage of arable land on the Loess Plateau and driven the development of the local economy (Figure 1e–f) [12]. On the other hand, however, the implementation of the GLCP has significantly altered the original topography of the project area and transformed land use patterns [19], resulting in significant changes in the hydrological ecosystem and thus inducing varying degrees of new natural and environmental hazards, such as erosion, soil salinization, and dam failure [20–22]. Due to the frequent occurrence of these disasters, large areas of newly created arable land in the watershed have not been effectively utilized, which seriously affects the normal operation of the GLCP [23].

The rapidly developing remote sensing techniques have been widely demonstrated to be useful tools for investigating geological hazards [15]. High-resolution satellite imagery provides comprehensive and intuitive ground information over large areas and can be used to characterize the spatial distribution patterns of surface hazards [24]. Many soil erosion models have been proposed to compensate for the complexity and infeasibility of measuring soil erosion rates on a regional scale, such as physically-based, empirical and semi-empirical models [25,26]. Compared to physically-based models with high requirements, cost, and complexity, the empirical-RUSLE (revised universal soil loss equation) has been widely used for soil erosion assessment at different scales, such as regional, catchment, watershed, and field scales, due to its robust model structure, moderate data requirements and high compatibility [27–30]. Although the RUSLE model does not consider all the complex interactions of sediment transport and deposition, it is widely used for soil erosion assessment at the plot and watershed scales in the Loess Plateau region because of its good ability to predict average annual erosion [31–34].

Several studies evaluated the effect of the GLCP on soil erosion using the RUSLE model and found that the GLCP significantly reduced soil erosion in the project area overall [35]. However, the GLCP exacerbated soil erosion in some areas, such as on the excavated slopes, field ridges, and natural grasslands. Exacerbated soil erosion in these areas is usually related to the topography, rainfall intensity, soil type, and vegetation cover remaining after slope excavation [36]. In addition, the large scope of the GLCP significantly changed the original hydrogeological environment within the watershed, which led to a significant rise in the groundwater table and production of soil salinization in the newly created arable land [12,37]. In addition to erosion and salinization, dam failures have also been widely reported following the implementation of the GLCP, which highlights the dominant roles of heavy rainfall and seepage erosion [38,39]. However, the spatial distribution patterns and interrelationships of the disasters that manifest following the completion of the GLCP are still unclear. Further research is needed to gain insight into the spatial distribution patterns and interrelationships of the post-GLCP disasters. This information will be beneficial for the improvement of the GLCP, disaster mitigation, and sustainable use of newly created arable land.

Figure 1. Site photos showing the process and local situation of the GLCP implemented in the Gutun watershed (GTW). (**a**) Original landform; (**b**) cutting foot slopes and filling gully channel; (**c**) building dams and reservoirs; (**d**) leveling farmland and planting cut slopes; (**e**) landscape of branch channel; (**f**) upstream landscape of #3 reservoirs and dam.

In this study, by means of remote sensing combined with geophysical exploration and field surveys, the distribution patterns and causative factors of hazards arising from the implementation of the GLCP within the Gutun watershed (GTW) have been examined, and hazard chains have also been discussed. The spatial distribution patterns of the three disasters were first investigated by remote sensing interpretation and field surveys. In addition, the RUSLE model was utilized to analyze the characteristics of erosion variability on spatial and temporal scales. Then, geophysical exploration methods were used to reveal the role of rising groundwater levels in controlling salinization. Next, the deformation and failure characteristics of silt dams were characterized in detail by using unmanned aircraft photogrammetry (UAV). Finally, the action process of the hazard chain was revealed by analyzing the spatial interconnection of three geological hazards. These results will better

contribute to disaster prevention and control as well as to the efficient implementation of subsequent large-scale land consolidation.

2. Study Area

The GTW (109°46′E to 109°52′E and 36°45′N to 36°51′N) is located in Baota District, Yan'an city, Shaanxi Province, approximately 46 km east of the old city of Yan'an (Figure 2). The total area of the GTW is approximately 42 km^2, which is a typical hilly and gully area within the Loess Plateau. The overall topography of the study area is high in the northwest and low in the southeast, with an average elevation of 1070 m. The GTW as a whole is covered by Quaternary loess. Furthermore, the GTW has a continental monsoon climate and a warm-temperate semi-arid climate zone, with an average annual temperature between 7.7 °C and 11.6 °C. In addition, the average annual rainfall in the GTW is approximately 500 mm, with an uneven rainfall distribution during the year. The rainfall in the GTW is mainly concentrated from July to September, with mostly sudden and heavy rainfall. However, the GTW has a high evaporation rate of up to 1000 mm/a, which is twice the annual rainfall [40].

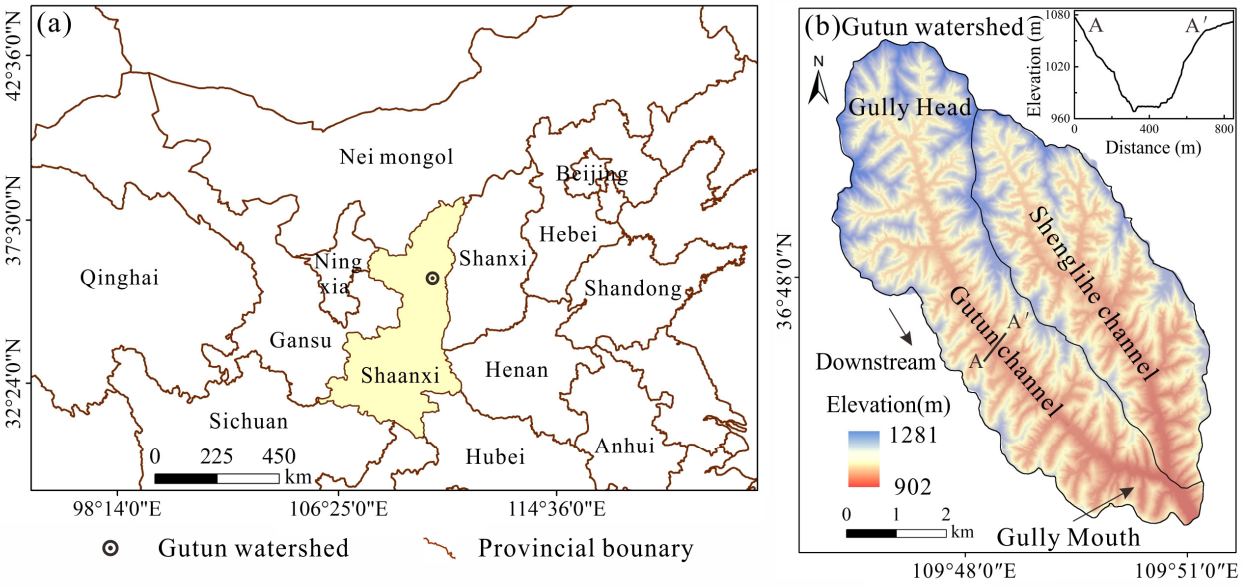

Figure 2. Location of the study area. (**a**) Location of the study area in Shaanxi Province; (**b**) topography of the Gutun watershed, including the two main channels of the Gutun and Shenglihe. The illustration in the upper right corner shows the topography of the A–A' profile.

The GTW has two major channels, the Gutun channel and the Shenglihe channel, and the topography of the main channel features a general "U" shape (Figure 2b). The GLCP was implemented in the GTW in 2012 and was completed in 2013. The GLCP creates new agricultural land by cutting the foot of slopes and backfilling the spoil into the gullies for local farmers (Figure 1). After the GLCP was completed in 2013, the area of relatively flat arable land increased by approximately 27.32 ha and was mainly concentrated in the gully area. In addition, five reservoirs and dams were built in the Gutun channel during the implementation of the GLCP for water storage and ecological enhancement of the watershed. A number of silt dams were built in the branch channels with the main purpose of retaining surface water and silting up eroded sediment to build up agricultural land. The project improved land utilization by providing new land use patterns while simultaneously enabling ecological improvements [41,42]. In general, the implementation of the GLCP has been widely recognized and supported within the GTW [43]. However, the GLCP has also significantly modified the original engineering and hydrogeological conditions, triggering a series of new hazards in the GTW, such as erosion, soil salinization, and dam failure, which severely limit the engineering benefits of the GLCP.

3. Data and Methodologies

3.1. Interpretation of Remote Sensing Images and Field Surveys

Overall, the GLCP has largely changed the land use pattern of the GTW, resulting in significant changes to the topography and eco-environment. In particular, unreasonable construction in some areas, combined with extreme external environmental conditions, such as heavy rainfall, has triggered geological hazards of varying degrees, such as soil erosion, salinization, and silt dam failure. Two optical images with spatial resolutions of 0.46 m and 0.48 m obtained from Google Earth on 2 October 2018 (Geoeye-1) and 4 October 2020 (WorldView-2) were selected and visually interpreted to obtain the basic characteristics of the GLCP and the spatial distribution patterns of surface geohazards such as soil salinization and dam failure. Field surveys were also conducted to verify the interpretation results. Examples of land use and disaster types identified through integrated remote sensing interpretation and field surveys are shown in Figure 3.

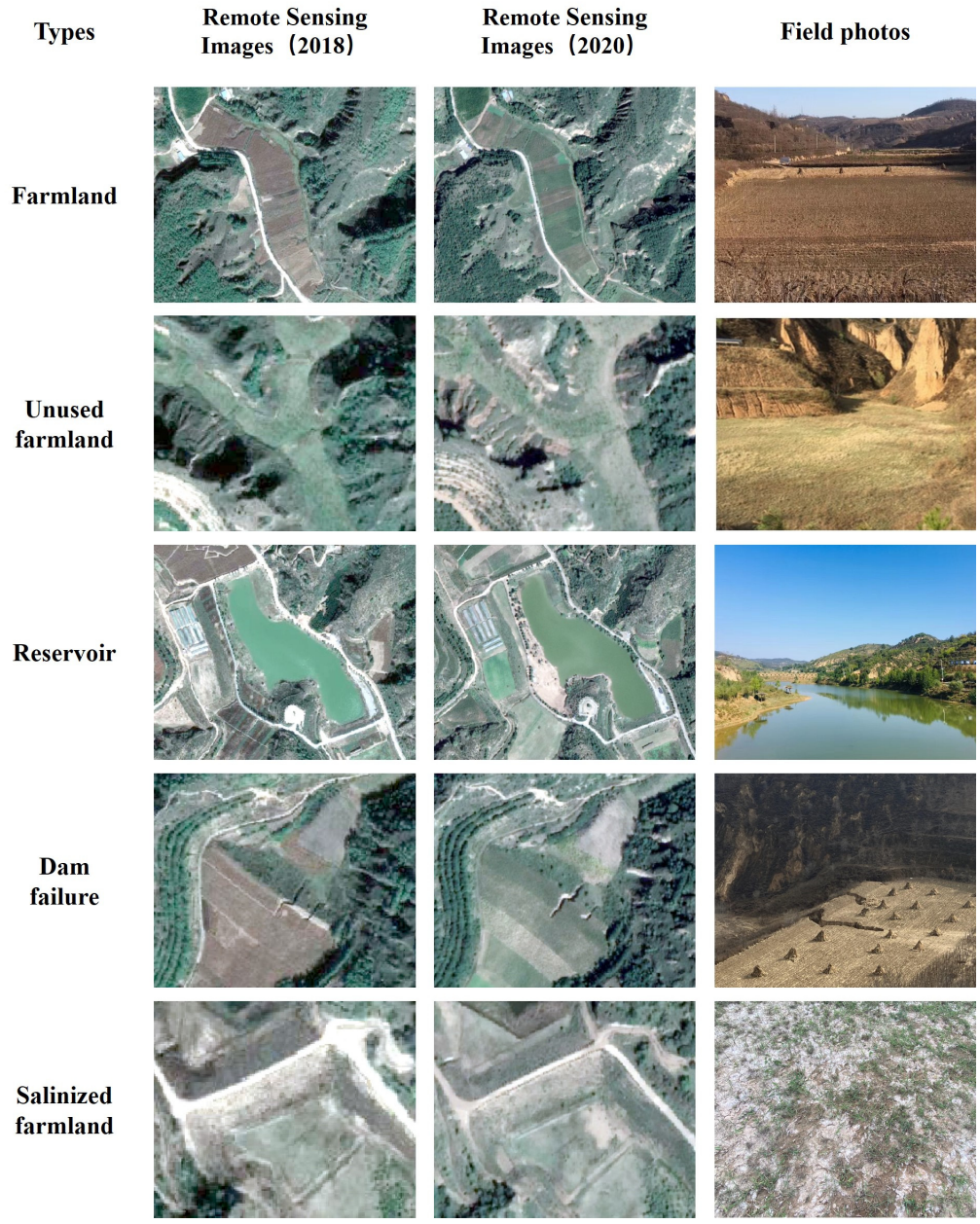

Figure 3. Examples of land use and disaster types identified by combining remote sensing images and field surveys.

3.2. Erosion

After completion of the GLCP, the GTW was subjected to severe erosion driven by extreme rainfall conditions due to the undulating topography. The RUSLE model, which was modified on the basis of the USLE (Universal Soil Loss Equation) [26,44,45], was selected to study the changes in erosion between 2018 and 2020 in the GTW. Although the empirically-based RUSLE model cannot reflect the complex interactions involved in soil erosion and consequently leads to limitations in accurately estimating soil erosion [28], its applicability and reliability in the Loess Plateau has been widely demonstrated in applications at different scales [31]. In addition, the main purpose of modeling in this study is to assess the relative changes in erosion risk in the GTW, so the RUSLE model results can provide a reasonable and accurate reference [29,30]. Detailed descriptions of the RUSLE model introduction, calculation, and processing have been extensively reported in previous studies [28,30]. The computational expression of the RUSLE model is:

$$A = R \cdot K \cdot LS \cdot C \cdot P \quad (1)$$

where A indicates the average annual soil erosion rate ($t \cdot hm^{-2} \cdot a^{-1}$); R is the rainfall erosivity factor ($MJ \cdot mm \cdot hm^{-2} \cdot h^{-1} \cdot a^{-1}$); K is the soil erodibility factor ($t \cdot h \cdot MJ^{-1} \cdot mm^{-1}$); LS is the topographic factor (dimensionless); C is the land cover factor (dimensionless); and P is the conservation practice factor (dimensionless). The result of Equation (1) is multiplied by 100 to obtain the international system unit ($t \cdot km^{-2} \cdot a^{-1}$). The spatial data with different resolutions used for the calculation were resampled to the same pixel size of 5 m × 5 m in the GTW using the nearest neighborhood method [46]. The annual soil erosion volume (t) is obtained by multiplying the average annual soil erosion rate by the eroded area.

The R-factor is a potential driver of rainfall-induced erosion [31]. Considering the small area of the GTW, the rainfall is assumed to be uniformly distributed; thus, the daily rainfall calculation method is used to calculate the R-factor [47]. Daily rainfall data were obtained from the meteorological station of Yan'an station. In this study, the R-factor was calculated using a method based on daily rainfall data proposed by Zhang and Fu (2003), which reduces the bias based on annual or monthly rainfall data and has been widely used in China [32,48,49]. This method is based on the accumulation of semi-monthly rainfall erosion erosivity, and its detailed calculation procedure can be found in previous reports [31,33,48].

The K-factor reflects the sensitivity of the soil to erosion. The erosion-productivity impact calculator (EPIC) model was selected for the study to calculate the K-factor [50]. The K value was converted from US customary units to international system units by multiplying by 0.1317 [28]. Soil property data were obtained from the Soil Science Database (SSD). Unlike most regions with complex soil type distribution characteristics [51], the GTW is small in area and covered by loess, so the spatial heterogeneity of soil properties is relatively small. The soil gradation is considered to be unchanged due to the absence of large-scale engineering activities in the GTW between 2018 and 2020.

The LS-factor usually reflects the effect of slope length (L) and slope gradient (S) on erosion and is the most important factor in determining the rates of erosion [26]. Considering that the maximum slope in the GTW exceeds 100% and the average slope is approximately 69%, the China Soil Loss Equation (CSLE) was chosen for the estimation of the LS factor [31,52–54]. A digital elevation model (DEM) with 10 cm spatial resolution obtained by UAV photogrammetry was used to estimate LS factors based on a flow accumulation algorithm to reduce bias in erosion estimation [30].

In addition, 10 land use types in the GTW between 2018 and 2020 were observed through remote sensing interpretation and field surveys. In this study, the C-factor (Table 1) and P-factor (Table 2) were determined according to different land use types and combined with the geomorphological characteristics of the GTW with reference to previous related studies [55,56].

Table 1. Parameters of the C-factor.

Land Use Types	Cropland	Residents, Hardened Pavement	Working Land, Nonhardened Pavement, Water Area, Bare Ground	Grassland	Woodland	Shrubland
C	0.28	0.9	1	0.09	0.004	0.02

Table 2. Parameters of the P-factor.

Slope (°)	Cropland	Grassland	Woodland, Nonhardened Pavement, Bare Ground, Working Land, Shrubland	Water Area, Residents, Hardened Pavement
0–1	1	1		
>1–9	0.3			
>9–18	0.5	0.8	1	0
>18–21	0.6			
>21	1	1		

Figure 4 shows the flow chart of the RUSLE model used to assess the soil erosion rate in the GTW. Since the processing procedures adopted for the RUSLE factors are all widely used and validated by field observations in similar loess areas, this paper does not focus on assessing the uncertainty and applicability of the model. It should be noted that the soil erosion rate derived from the RUSLE model should be considered the best available estimate rather than an absolute value since all complex interactions associated with soil erosion are not considered [57]. Furthermore, due to the number and identical nature of the data sets, the relative changes in the model estimates for the two periods can be seen as having a high consistency and reliability [29].

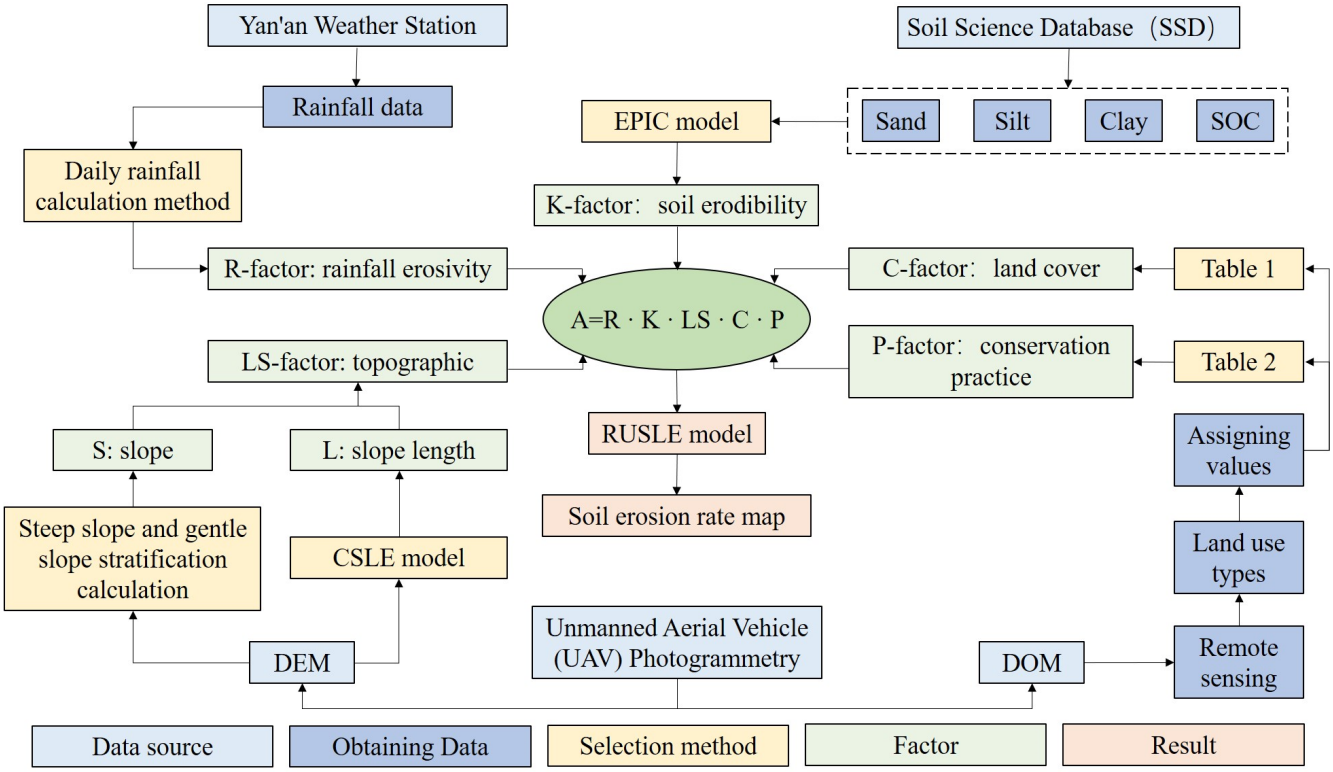

Figure 4. Calculation method and parameter values of the RUSLE model. All factors and abbreviations are defined in the text.

3.3. Salinization

The large-scale implementation of the GLCP has dramatically changed the original hydrogeological environment in the GTW, leading to a rise in the groundwater table of the newly created farmlands, which makes the loess farmland rich in soluble salts susceptible to salinization [12]. During the field survey, severe salinization, consisting of salt precipitate, was widely observed on the surface of the arable land in the gully after the GLCP. It is obvious that crops cannot be cultivated on salinized arable land, which results in large areas of newly created arable land not being able to be used properly (Figure 5b,c). The farmland with visible salt precipitation on the surface was visually interpreted using Google Earth images with a spatial resolution of 0.48 m collected in October 2020, and field surveys were conducted to verify the interpretation results. The interpretation results were used to characterize the spatial distribution of salinized farmland in the GTW. Hydrological analysis was also performed to reveal the spatial control factors of salinized arable land.

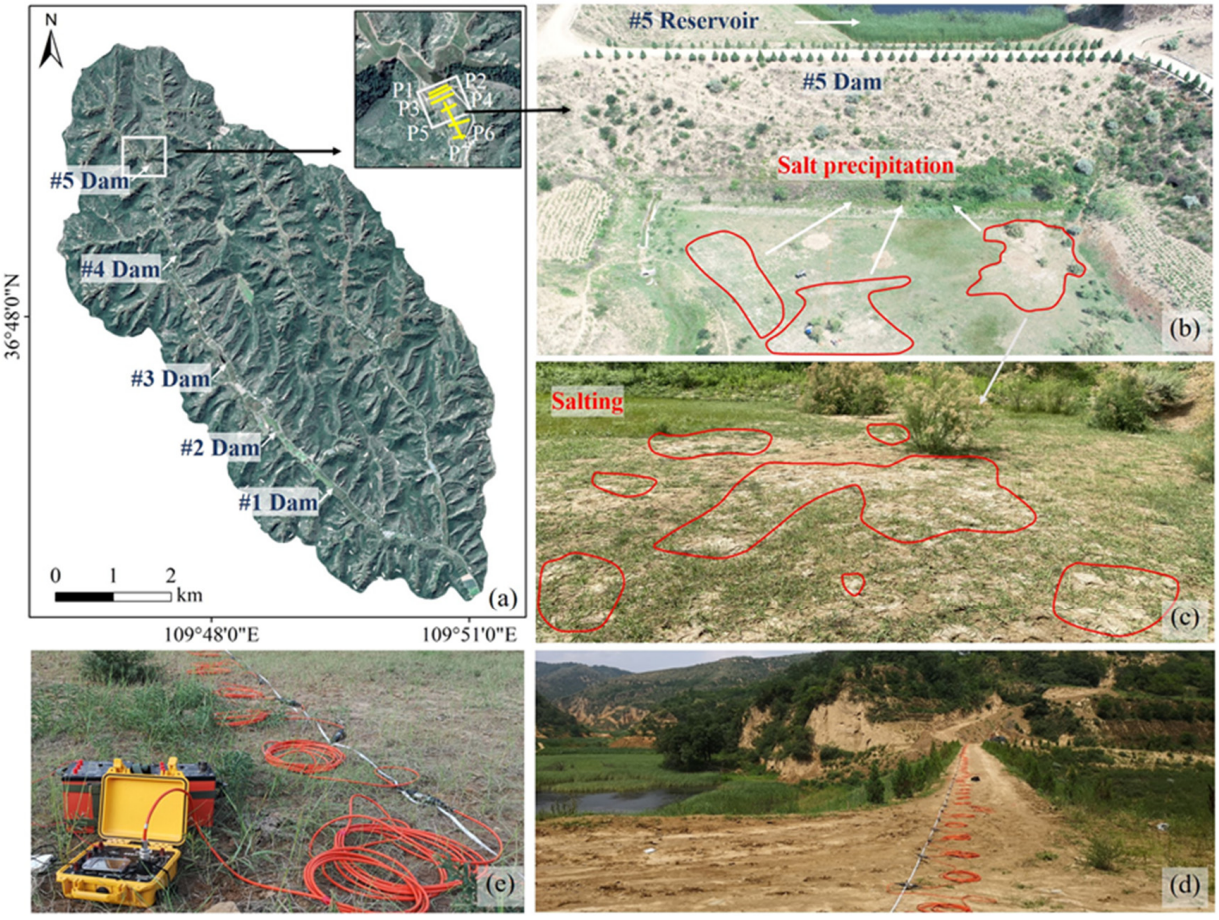

Figure 5. Layout of ERT profiles and field photos. (**a**) Remote sensing image map of the GTW showing the location of the five dams and the ERT profile; (**b**) site map of the #5 reservoir and #5 dam, with salinized arable land downstream of the dam; (**c**) local photo of salt precipitate on farmland located downstream of the #5 dam; (**d**) site photo of the P2 profile; (**e**) ERT fieldwork photo.

The #5 dam is located upstream of the GTW channel. The field survey found that the arable land downstream of the #5 dam is severely salinized, resulting in a large area of abandoned farmland (Figure 5). To study the cause of the typical salinization of the arable land downstream of the dam, the electrical resistivity tomography (ERT) method was used in the field to examine the hydrological characteristics before and after the dam and in the arable land (Figure 5d). ERT can reflect the subsurface structure and regional hydrological information by measuring the potential difference of electrodes inserted into the soil, which has been widely used for groundwater level detection in loess areas [58,59].

The resistivity of the soil can be regarded as an indicator of the heterogeneity of the soil's physical properties [60]. Theoretically, water can be regarded as a good conductor of electricity, and air can be regarded as an insulator, so when there is a large difference in the water content and pore space in the soil, the water table can be differentiated based on significant differences in apparent resistivity measured by ERT. In addition, previous work has shown that slight differences in salt content in loess have little effect on the resistivity of loess relative to water content [61]. Thus, the ERT method allows us to explore the characteristics of groundwater distribution and the causes of soil salinization in the GTW.

In this case, a total of six transverse ERT profiles (P1–P6) and one longitudinal ERT profile (P7) were arranged upstream and downstream of the #5 dam, and the locations of the profiles are shown in Figure 5a. A total of 40 electrodes were deployed along each transverse ERT profile with an electrode spacing of 1.5 m, and the cumulative length of the six transverse profiles was approximately 360 m. In addition, 40 electrodes were also deployed in the longitudinal profile with an electrode spacing of 3.5 m, and the cumulative length was approximately 140 m. ERT measurements were obtained using a Wenner device (Figure 5e), which offers good resolution. Res2Dinv software was utilized to conduct the inversion of the apparent resistivity, and at least 2 iterations of calculations were performed to reduce the fitting error. In addition, to verify the ERT sounding results, a manual drilling borehole (Luoyang shovel) was conducted at the junction of the P6 and P7 profiles to determine the soil water content at different depths.

3.4. Dam Failure

The construction of silt dams is more widely implemented in loess areas. The GLCP leveled the arable land in the gully and built a large number of silt dams between the arable land in the branch gully (Figure 1e). Silt dams are generally distributed on the drainage channels of each branch gully channel and are used to reduce and mitigate the impact of soil erosion on farmlands [62]. Specifically, silt dams can be used in gullies to accumulate surface water for cultivation and to capture eroded sediments in areas of severe soil erosion, thus retaining the sediments for use on arable land. In the GTW, there are approximately five silt dams positioned between farmland from the upstream to downstream locations in each branch gully.

However, the inadequate design of the silt dam, combined with extreme external rainfall conditions, led to the destabilization of the loess dam foundations and even the destruction of the silt dams. A large number of silt dams that have failed in some of the branch gullies within the GTW were located and observed during field investigations. Dam failure was a typical geohazard in the GTW after the completion of the GLCP. Two optical images acquired from Google Earth in 2018 and 2020 were used to visually inspect the failed dams for comparison with field observations, and the interpretation results were used to study their distribution characteristics and patterns. In addition, a typical case of a silt dam that broke on 21 August 2018 was selected for specific study and analysis (Figure 6). The area upstream of the silt dam is a reservoir with sufficient water storage capacity, and the downstream part consists of agricultural land. It is noteworthy that there was no waterproofing measure in the silt dam. A crack gauge was installed on the top of the dam to monitor displacement on 8 July 2018, after the first localized collapse of the dam. Furthermore, DOM and DEM data with a resolution of 10 cm were acquired by UAV photogrammetry techniques on July 15 and 7 November 2018, to explore the deformation failure characteristics of the silt dam in detail (Figure 6e).

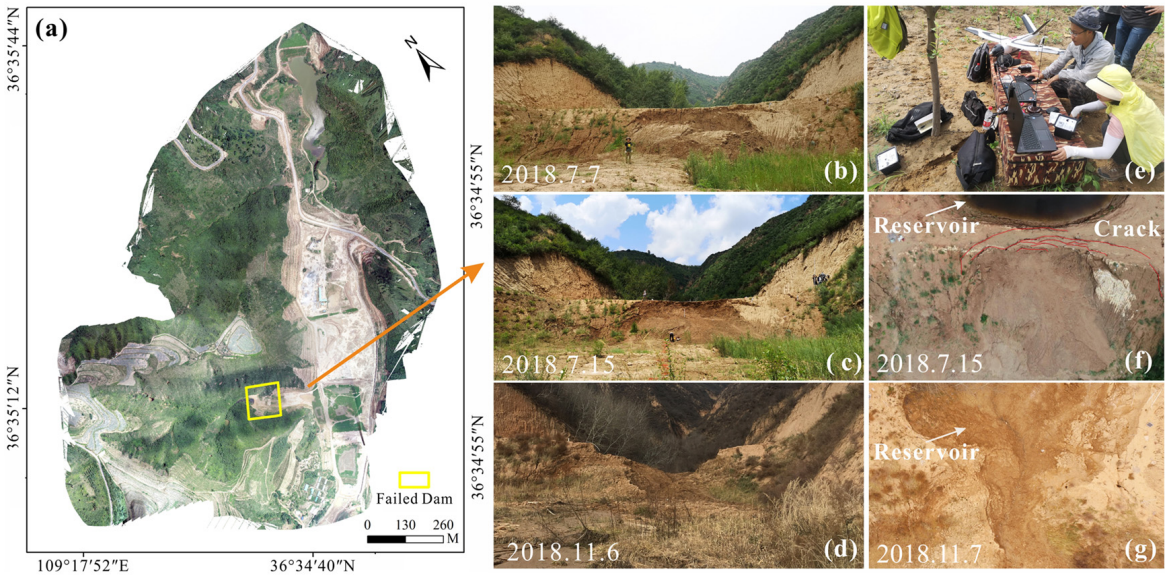

Figure 6. DOM and site pictures of a typical failed dam case. (**a**) DOM of the failed dam area obtained by UAV photogrammetry; (**b**–**d**) photos downstream of the dam at different times; (**e**) field work photos of UAV photogrammetry; (**f**) top view of the silt dam on 15 July 2018; (**g**) top view of the silt dam on 7 November 2018.

4. Results

4.1. Soil Erosion Characteristics

The average soil erosion rate of the watershed was first obtained by superimposing the erosion factors on the RUSLE model. Then, soil erosion was classified into six classes according to the Soil Erosion Classification and Grading Standard: micro, mild, moderate, intense, extreme, and severe erosion. Figure 7a,b shows the soil erosion intensity classification maps for the GTW in 2018 and 2020, and Table 3 shows the results of the soil erosion classification statistics.

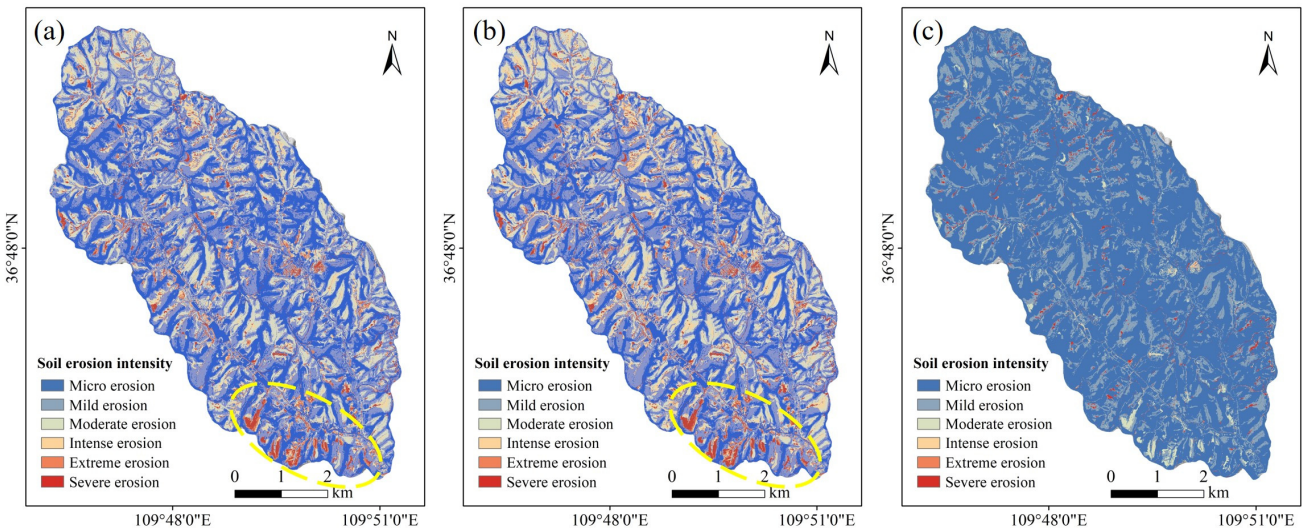

Figure 7. Soil erosion intensity classification map of the GTW obtained after applying the RUSLE model. (**a**) Soil erosion intensity classification map for the GTW in 2018; (**b**) soil erosion intensity classification map for the GTW in 2020; (**c**) change in soil erosion intensity from 2018 to 2020. The yellow dashed outlines in panels (**a**,**b**) highlight areas of severe erosion.

Table 3. Classification statistics of soil erosion intensity in the GTW in 2018 and 2020.

Erosion Classification	Average Soil Erosion Rate ($t \cdot km^{-2} \cdot a^{-1}$)	Area (km^2)			Average Annual Soil Erosion Rate ($t \cdot km^{-2} \cdot a^{-1}$)			Erosion Volume (t)		
		2018	2020	Change	2018	2020	Change	2018	2020	Change
Micro-erosion	≤500	14.41	12.46	−1.95	185.49	230.94	45.45	2661.41	2877.1	215.69
Mild erosion	>500–2500	15.22	15.45	0.23	928.92	955.4	26.48	14,136.84	14,758.6	621.76
Moderate erosion	>2500–5000	8.3	8.46	0.16	2828.39	3137.96	309.57	23,649.1	26,541.55	2892.45
Intense erosion	>5000–8000	1.5	2.61	1.11	4776.96	5140.75	363.79	7184.79	13,439.46	6254.67
Extreme erosion	>8000–15,000	0.9	0.91	0.01	8972.74	9542.76	570.02	7458.02	8746.18	1288.16
Severe erosion	>15,000	1.64	1.86	0.22	36,400.7	67,766.6	31,365.9	46,104.12	126,018.9	79,914.78

The results calculated by the RUSLE model showed that, overall, the GTW suffered from mild erosion in 2018, with an average soil erosion rate of 2423.57 $t \cdot km^{-2} \cdot a^{-1}$ and a total erosion of 101,194.29 t. The average soil erosion rate in 2018 was slightly lower than the previous assessment of 2857.76 $t \cdot km^{-2} \cdot a^{-1}$ in a similar loess area (Beiluo River basin) using the RUSLE model [31]. In 2020, the overall erosion intensity of the GTW increased significantly to moderate erosion, with an average soil erosion rate of 4583.79 $t \cdot km^{-2} \cdot a^{-1}$ and a total erosion of 192,381.75 t. Apparently, the average soil erosion rate in the GTW increased by 2160.22 $t \cdot km^{-2} \cdot a^{-1}$ from 2018 to 2020, and the total erosion increased by 91,187.46 t. It should be noted that the dominant erosion type in the GTW during both 2018 and 2020 was micro- and mild erosion, with proportional areas of 70.61% and 66.83%, respectively. The proportional area of the severely eroded area in the GTW in 2018 and 2020 was relatively small at 3.91% and 4.46%, respectively, and was mainly distributed along the slopes at the gully mouth of the Gutun channel, as shown in the yellow dashed outline in Figure 7a,b. In addition, the area of micro-erosion in the watershed changed most significantly from 2018 to 2020, decreasing by 4.51%, while the area of intense erosion increased by 2.69%.

It should be noted that the RUSLE model does not consider all erosion types, and therefore the model estimates are subject to some uncertainty [28]. However, given the same quality and nature of the input data, the relative changes in the model estimates for 2018 and 2020 are significantly informative [29,30].

4.2. Regional Salinization

The distribution of salinized farmland in the GTW was obtained by remote sensing interpretation and field verification, as shown in Figure 8. The entire GTW covers an area of 4200 ha, of which the farmland area reached 328.58 ha in 2020 after the implementation of the GLCP, and the unutilized farmland area was 34.5 ha, accounting for 10.5% of the farmland area of the GTW. In addition, up to 195 salinated areas were distributed throughout the arable land of the GTW, for a total area of 9.42 ha, accounting for 2.9% and 27.3% of the total area of arable land and unused arable land, respectively. It is worth noting that the salinized arable land that was visually inspected only represents arable land with severe salinization and clear evidence of salt precipitation on the surface. Although many areas adjacent to the inspected salinized farmland have no obvious salt particles on the surface, the farmland has suffered salinization, which makes it difficult to grow crops and is thus not utilized.

Furthermore, the kernel density distribution of sites where salt precipitation was observed in the GTW was obtained by density calculation in the spatial analysis tool within the ArcGIS environment (Figure 8b). It was found that there are four main areas of concentrated salinization in the GTW, mainly located at the gully mouth and gully head areas of the Gutun channel and the gully head areas of the Shenglihe channel. Concentrated rainfall in the GTW occurs mainly during the summer months and is dominated by sudden and heavy rainfall, which leads to surface water pooling in relatively flat valley farmland areas and raises the groundwater table. In addition, there is less human activity in the gully head area, which makes the arable land in this area more susceptible to salinization due to the absence of human intervention. Within the Gutun channel, severe soil salinization

occurred mainly in the farmland downstream of the dam that was in front of the five reservoirs, and the leakage of reservoir water may play an important role in salinizing the farmland downstream of the dam.

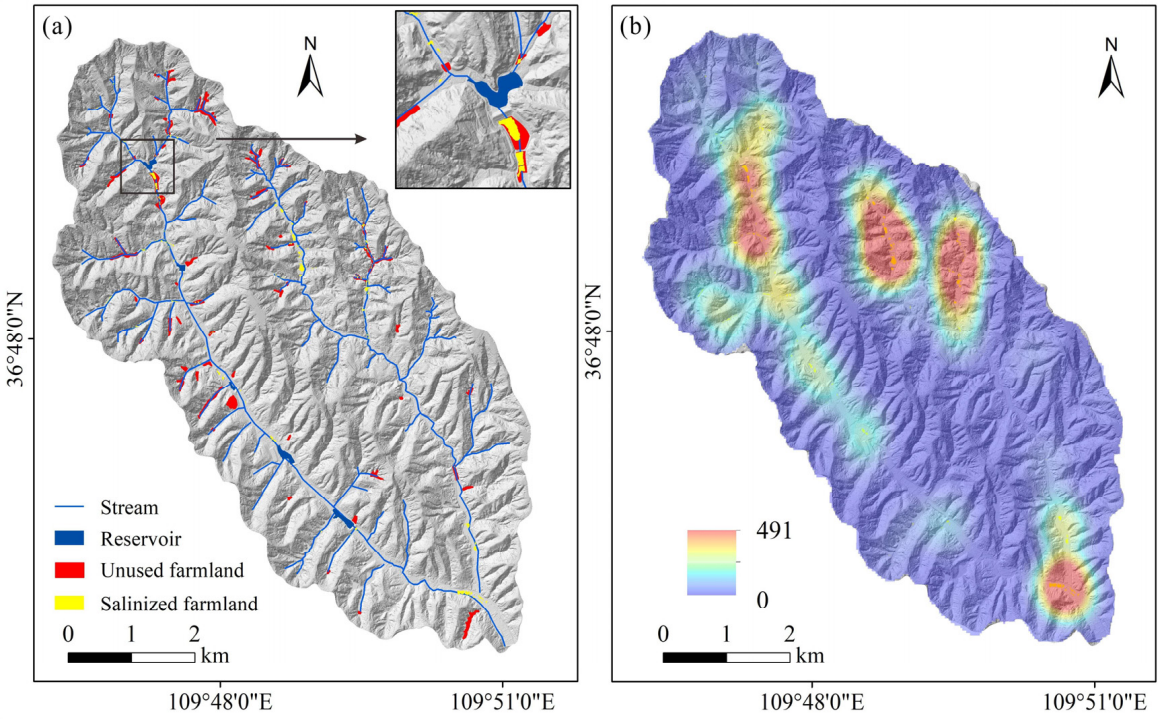

Figure 8. Spatial distribution map of salinization in the GTW. (**a**) Map of unused arable land and arable land where salt precipitate was observed in the GTW, which also includes water systems and reservoirs in the GTW; (**b**) kernel density distribution of salinized arable land in space.

4.3. Distribution Characteristics of Dam Failure

The spatial distribution of all dams and failed dams, mapped by visual interpretation and detailed field investigation, is shown in Figure 9a. After the GLCP, a total of 238 new silt dams were built in the GTW, with approximately 206 of them concentrated in the branch channels. Generally, it seems that the dam failure hazards are mainly distributed in each branch channel, and the main central trench is largely free of the failed dam hazards, as shown in Figure 9. In 2018, a total of 20 failed silt dams were observed in the GTW, mostly concentrated in the branch ditches at the gully mouth of the Gutun channel (Figure 9b). In the GTW, the largest area of the failed silt dam reached 540.83 m^2, the smallest area reached 31 m^2, and the average area of the failed dam was 164 m^2. In 2020, a total of 59 silt dams failed (Figure 9c), mainly in the branch gully channels and at the gully mouth locations of the Gutun channel. The largest failed dam area reached an area of 861.19 m^2, and the smallest area was 17.7 m^2, with an average area of 142 m^2. From 2018 to 2020, the spatial distribution density of failed dams in the GTW tended to increase, with the most significant increase in the areas located in the gully head and gully mouth of the Gutun channel and in the branch gullies on both sides of the Shenglihe channel (Figure 9d). Additionally, field investigations revealed that all silt dams in some of the branch ditches failed, which was mostly attributed to the concentrated heavy rainfall in the 2020 rainy season. When the silt dam failed, the depth of the failure was usually 2–3 m, and the width was approximately 3 m. After the dam failed, the arable land downstream of the silt dam was severely affected, resulting in the destruction of some crops. A large amount of surface water even accumulated in the downstream arable land and could not be drained in time, which had a large impact on crop cultivation.

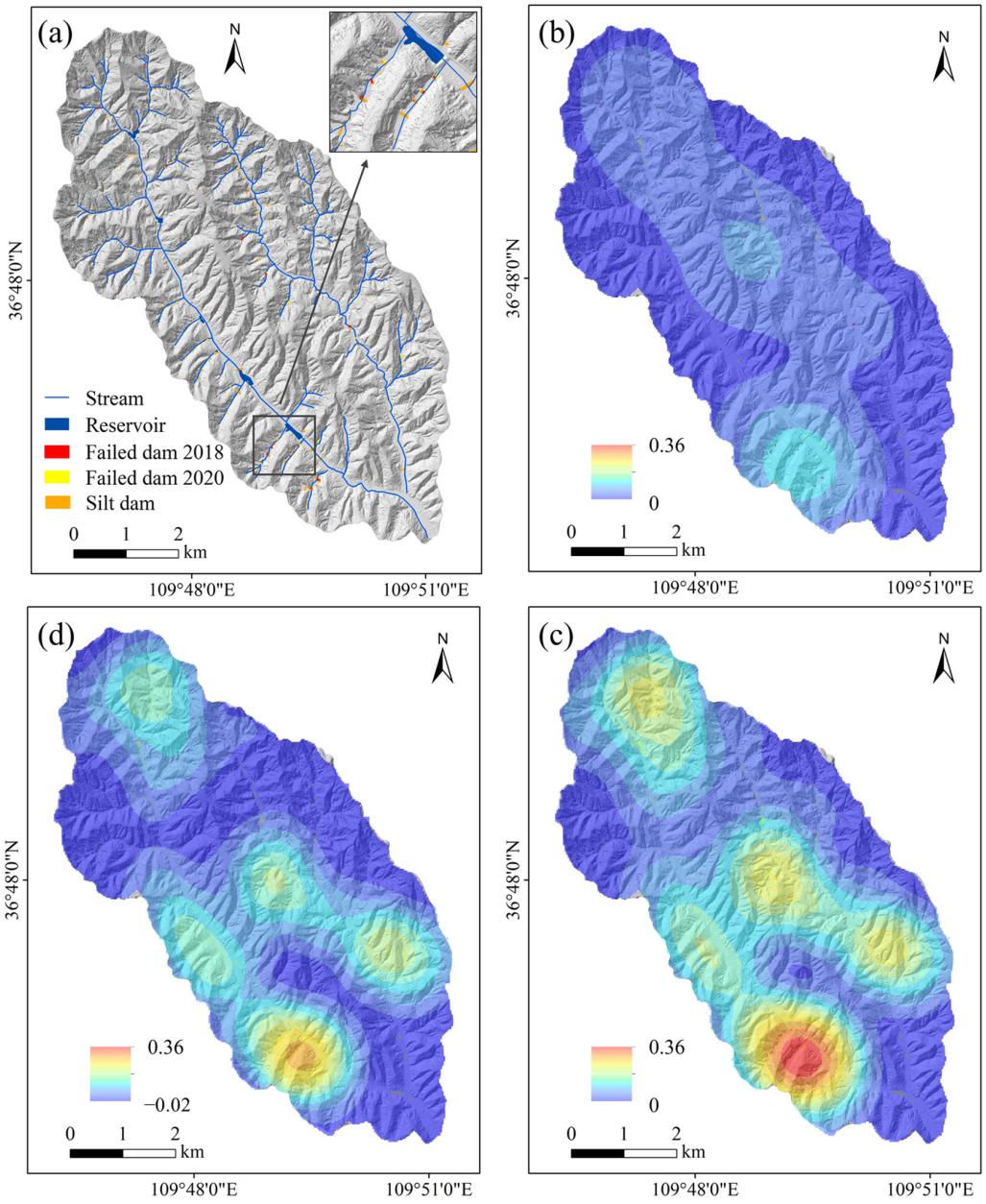

Figure 9. Spatial distribution map of the failed dam. (**a**) Spatial distribution of the failed dams in 2018 and 2020; (**b**) kernel density distribution of failed dams in 2018; (**c**) kernel density distribution of failed dams in 2020; (**d**) changes in the kernel density distribution of failed dams from 2018 to 2020.

5. Discussion

5.1. Changes in Erosion

Of the five factors considered by the RUSLE model, the implementation of the GLCP directly influenced all but the R-factor. The excavation and backfilling undertaken during the GLCP occurred within the GTW; thus, the change in the K-factor was minimal, while the change in the LS-factor was significant. The C-factor and P-factor mainly varied with land use pattern. Soil erosion changes in the GTW in 2018 and 2020 were further examined by grading statistics of slope, slope aspect, and elevation, and these findings can inform current erosion mitigation strategies in the GTW.

Erosion in the GTW is classified into six classes in terms of slope. In 2018, the average soil erosion rate increased with increasing slope within the GTW, peaking at the >35° slope zone (Table 4). In 2020, the average soil erosion rate showed a trend of increasing and then decreasing with increasing slope in the GTW, with peak erosion occurring in the >8–15°

slope zone. The most significant change in the average soil erosion rate in the watershed from 2018 to 2020 was in the >8–15° slope zone, increasing from 2378.24 t·km^{-2}·a^{-1} to 7984.44 t·km^{-2}·a^{-1}, which was mainly because corresponding vegetation restoration measures were not implemented in time following slope excavation in this slope zone. In addition, the >15–35° slope zone decreased from 2018 to 2020 in terms of area and erosion share, which could be attributed to the increase in the area of woodland and shrubland in this slope zone (Figure 10b). Conversely, the area and erosion share of the >35° slope zone increased by 9.76% and 1.82%, respectively, mainly due to the higher hydrodynamic conditions caused by the larger slope drop.

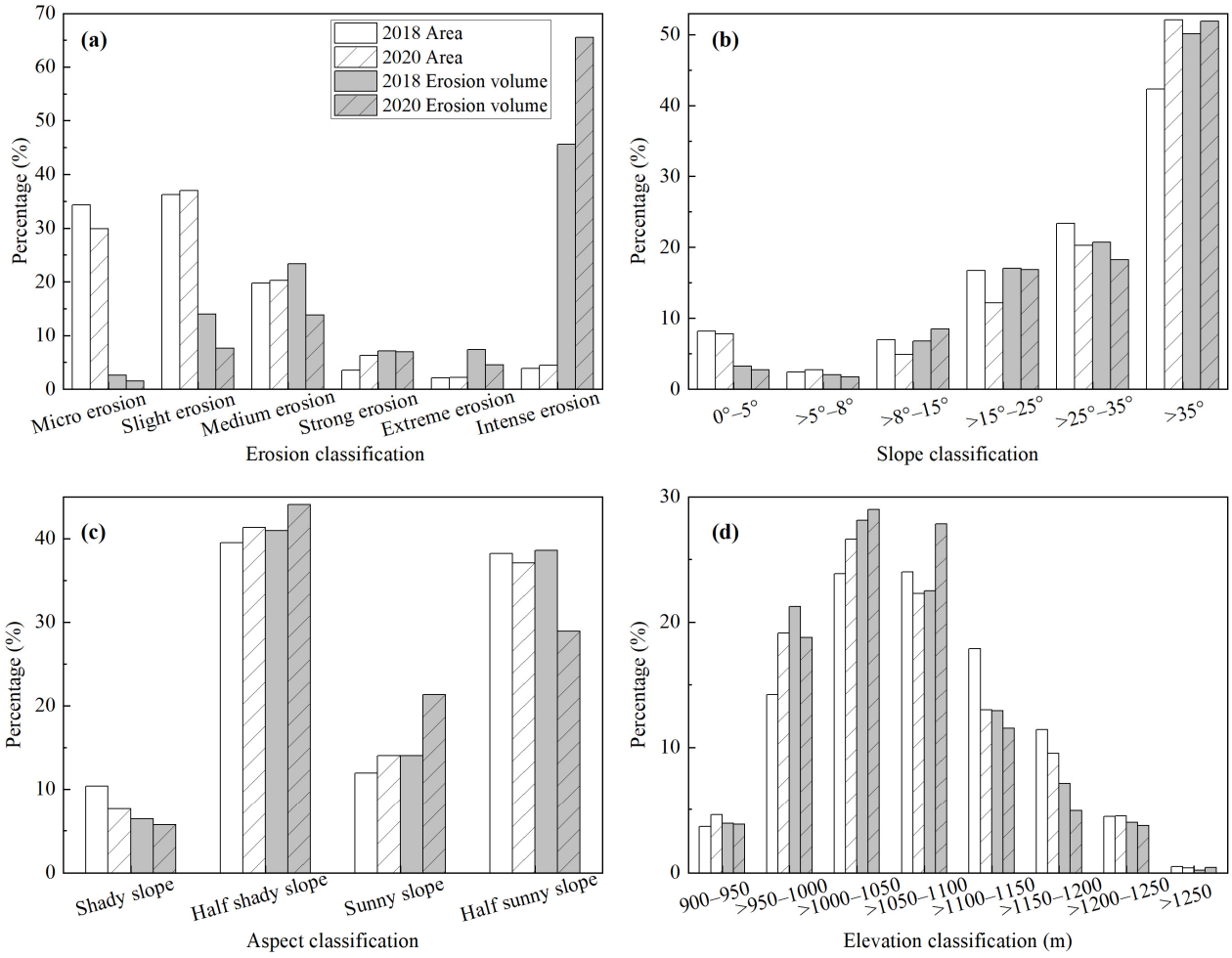

Figure 10. Comparison of soil erosion under different classifications. (**a**) Erosion classification; (**b**) slope classification; (**c**) aspect classification; (**d**) elevation classification.

Erosion in the GTW is divided into four classes in terms of aspect (Table 4). These are shady slopes (>337.5–22.5°), half-shady slopes (>22.5–157.5°), sunny slopes (>157.7–202.5°), and half-sunny slopes (>202.5–337.5°). In both 2018 and 2020, the maximum average soil erosion rate of the GTW was found on the sunny slopes, with rates of 2848.51 t·km^{-2}·a^{-1} and 7009.55 t·km^{-2}·a^{-1}, respectively. In terms of the average soil erosion rates, the most intense rates of soil erosion in the GTW occurred on sunny slopes, followed, in descending order, by half-shady slopes, half-sunny slopes, and finally shady slopes (where the erosion rate was the lowest). This finding is consistent with the observations of previous work using the RUSLE model in another typical watershed on the Loess Plateau [31]. The topography of the GTW was mainly dominated by half-sunny and half-shady slopes, and the area share in these two aspects was 77.71% and 78.42% in 2018 and 2020, respectively, corresponding to 79.85% and 72.98% of the total soil erosion volume (Figure 10c).

Table 4. Statistical table of soil erosion under different classifications.

Classification	Erosion Indicators	Average Annual Soil Erosion Rates ($t \cdot km^{-2} \cdot a^{-1}$)		Area (km^2)			Area Share (%)	Erosion Volume (t)			Percentage of Erosion Volume (%)
		2018	2020	2018	2020	Change	Change	2018	2020	Change	Change
Slope	0–5°	968.24	1630.73	3.41	3.25	−0.16	−0.38	3298.93	5296.89	1997.96	−0.51
	>5–8°	2054.55	2921.67	1.01	1.14	0.13	0.3	2084.6	3334.55	1249.95	−0.33
	>8–15°	2378.24	7984.44	2.9	2.05	−0.85	−2.03	6901.45	16,396.04	9494.59	1.7
	>15–25°	2472.79	6367.48	6.99	5.08	−1.91	−4.56	17,283.98	32,369.79	15,085.81	−0.25
	>25–35°	2144.84	4145.08	9.77	8.48	−1.29	−3.09	20,947.22	35,136.19	14,188.97	−2.44
	>35°	2867.29	4591.4	17.67	21.75	4.08	9.76	50,678.1	99,848.3	49,170.2	1.82
Aspect	Shady slope	1499.53	3469.26	4.33	3.16	−1.17	−2.8	6486.55	10,948.89	4462.34	−0.72
	Half-shady slope	2513.13	4911.51	16.5	17.25	0.75	1.82	41,459.3	84,747.57	43,288.27	3.08
	Sunny slope	2848.51	7009.55	4.98	5.85	0.87	2.1	14,177.32	41,023.53	26,846.21	7.31
	Half-sunny slope	2448.94	3594.19	15.95	15.49	−0.46	−1.12	39,071.11	55,661.76	16,590.65	−9.68
Elevation (m)	900–950	2596.21	3820.11	1.52	1.92	0.4	0.94	3956.7	7324.52	3367.82	−0.1
	>950–1000	3617.47	4525.71	5.94	7.99	2.05	4.9	21,493.67	36,150.38	14,656.71	−2.45
	>1000–1050	2858.49	5019.27	9.96	11.11	1.15	2.76	28,465.95	55,753.71	27,287.76	0.85
	>1050–1100	2272.16	5758.81	10.03	9.3	−0.73	−1.73	22,778.83	53,572.28	30,793.45	5.34
	>1100–1150	1750.28	4094.1	7.47	5.43	−2.04	−4.9	13,074.3	22,210.99	9136.69	−1.37
	>1150–1200	1509.7	2367.02	4.77	3.983	−0.787	−1.89	7205.03	9426.27	2221.24	−2.23
	>1200–1250	2177.38	3838.93	1.85	1.86	0.01	0.04	4027.53	7157.83	3130.3	−0.26
	>1250	920.96	4841.35	0.21	0.16	−0.05	−0.11	192.27	785.77	593.5	0.22

The erosion of the GTW is divided into eight classifications based on elevation (Table 4). Overall, it appears that, between 2018 and 2020, the average soil erosion rate in the watershed tended to increase and then decrease with increasing elevation, with peak erosion occurring at elevations of >1000–1100 m. The erosion intensity in 2020 was, for each elevation classification in the GTW, one grade more severe than what it was in 2018. In the GTW, the largest share of erosion volume was observed in the >1000–1050 m elevation zone, accounting for 28.13% in 2018 and 29.98% in 2020, which was mainly due to the sparse vegetation cover in this elevation area. The smallest share of erosion volume was observed in the >1250 m elevation classification, with only 0.19% in 2018 and 0.41% in 2020. This was mainly attributed to low human activities and high vegetation cover.

Except for topography-related factors, rainfall is usually an important driver of soil erosion. The cumulative rainfall in the GTW was 572 mm and 582 mm in 2018 and 2020, respectively, with maximum daily rainfalls of 40.9 mm and 80.3 mm, respectively (Figure 11). Although the cumulative rainfall in 2018 and 2020 was comparable, the annual rainfall erosivity (R-factor) estimated using daily rainfall data was 1761.6 MJ·mm·hm^{-2}·h^{-1}·a^{-1} and 2052.4 MJ·mm·hm^{-2}·h^{-1}·a^{-1}, both of which are higher than the Chinese average rainfall erosivity of 1600 MJ·mm·hm^{-2}·h^{-1}·a^{-1} previously reported [49]. The slightly greater annual rainfall erosivity in 2020 than in 2018 is an important controlling factor for the increase in soil erosion.

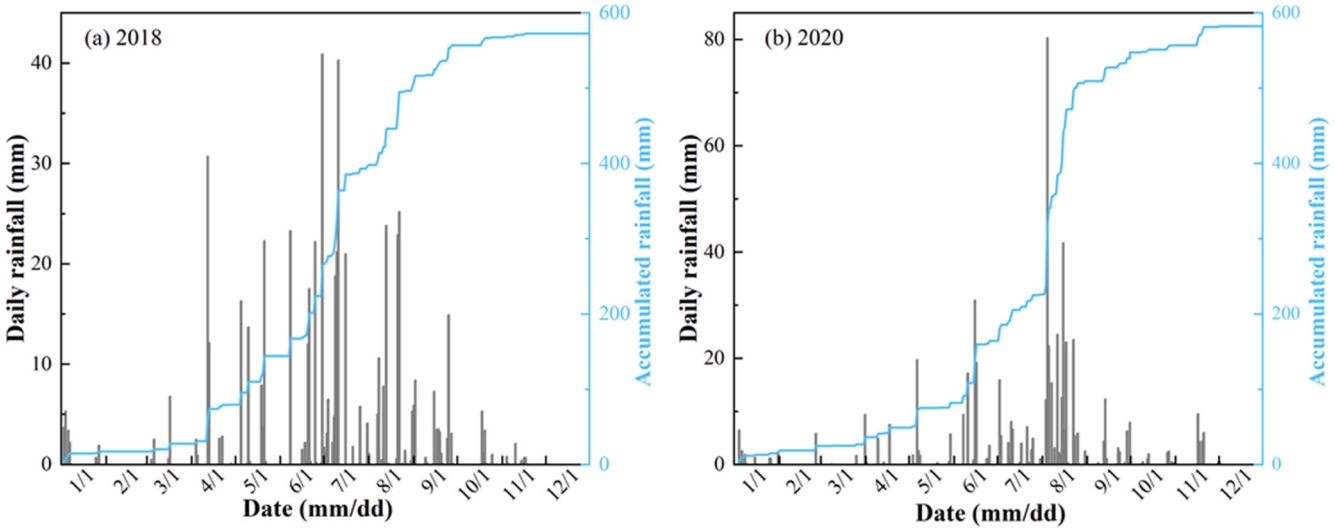

Figure 11. Daily rainfall in the Gutun watershed in 2018 (**a**) and 2020 (**b**).

5.2. Salinization Formation Mechanism

The field survey and hydrological analysis showed that two main factors contribute to the salinization of arable land within the GTW (Figure 12a). On the one hand, the outfalls of water systems within the watershed have a significant controlling effect on the spatial distribution of the salinized arable land. Hydrological calculations revealed that 90.77% of the salinized areas were mainly located in arable land near the main outfalls of the water system. A large volume of surface water accumulates on the surface at these locations due to outfalls, and the lack of timely discharge of surface water and the resultant rise in groundwater level may be the main cause of the soil salinization of these arable lands. The average soluble salt concentration in the loess parent material used for the GLCP in the GTW is as high as 0.87 g/kg, and the main anions and cations are HCO_3^- and Na^+, respectively, which provide an important material source for soil salinization [12]. In addition, the concentration of soluble salts in the water sources gradually increases due to the high evapotranspiration caused by the climatic conditions in the area where the GTW is located. When this water evaporates, salt is precipitated onto the surface of the arable land, resulting in salinization [12,63].

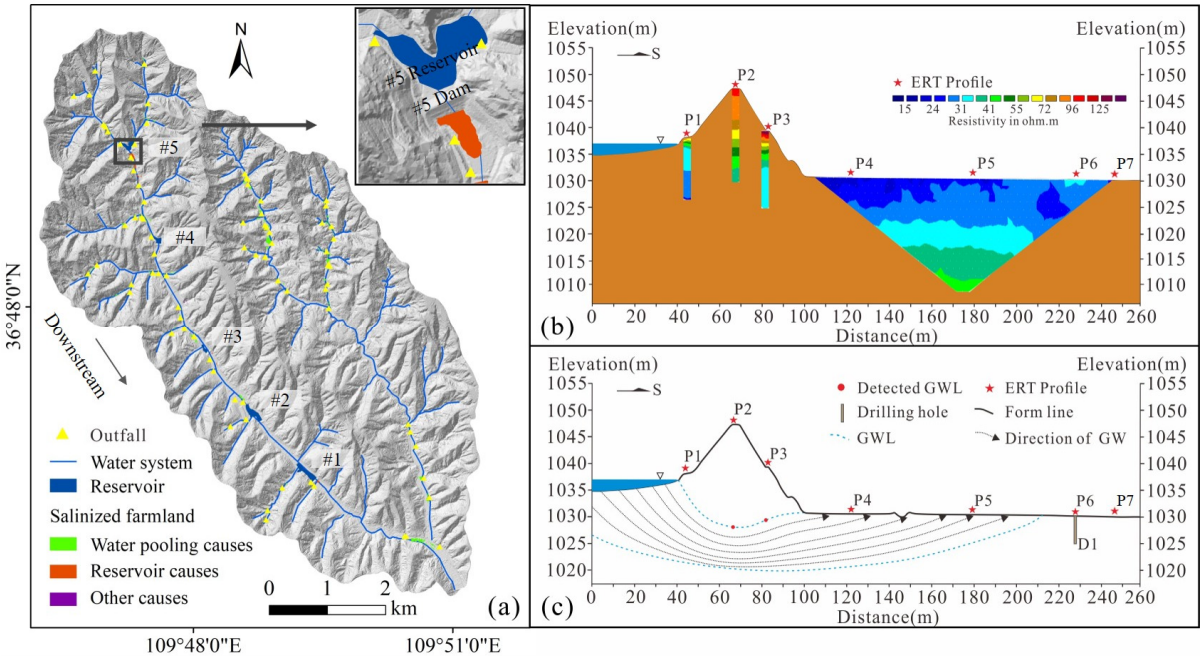

Figure 12. Distribution and causative patterns of salinized arable land. (**a**) Distribution map of land where salt precipitates were observed, and the top right graph shows the salinized arable land downstream of the #5 reservoir and #5 dam in greater detail; (**b**) results for 7 ERT profiles; (**c**) groundwater seepage pattern of the #5 dam; GWL: Groundwater level; GW: groundwater.

On the other hand, approximately 6.77% of the salinized area is located in the arable land downstream of the dams that are in front of the five reservoirs in the Gutun channel. The five reservoirs and dams were built during the GLCP for water storage and ecological enhancement of the watershed (Figure 12a). Among these, the #1 reservoir and dam are located the furthest downstream of the Gutun channel. The dams and reservoirs are numbered consecutively in the upstream direction, with the #5 reservoir and dam located the furthest upstream. There is a large difference between the reservoir water level and the groundwater level (GWL) of the arable land downstream of the dam, and the water level difference increases in the upstream direction of the Gutun channel. This water level difference may lead to the leakage of reservoir water along the bottom of the dam and thus cause the groundwater level of the arable land downstream of the dam to rise, which is usually the main reason for soil salinization in the Loess Plateau [12,64]. As this is a common and serious geohazard within the GTW in the wake of the GLCP, it is paramount to evaluate and investigate in detail the causes of arable land salinization downstream of the dam.

The arable land downstream of the #5 dam was found to be the largest area of salinization in the field survey and remote sensing analysis, and it was selected for detailed study utilizing geophysical exploration methods. After iterative calculations, the fitting error root mean square (RMS) of the seven ERT profiles ranged from 0.39–2.2%. Furthermore, by comparing the apparent resistivity measured by ERT with the soil water content measured by the field borehole, there is a significant negative correlation between apparent resistivity and water content. In our previous experimental results, it was shown that a small difference in salt content around the #5 dam had little effect on the variation in apparent resistivity compared to water content [61]. Therefore, the apparent resistivity is simply interpreted as the variation in water content in this paper.

Through ERT detection, it was found that the apparent resistivity around the #5 dam ranged from 0 to 120 Ωm (Figure 12b). In general, the apparent resistivity profile shows obvious horizontal stratification within the dam, and the apparent resistivity gradually decreases from the top to the bottom of the dam. The water content of the soil at the

top surface of the #5 dam is relatively low, with an apparent resistivity of approximately 100 Ωm. However, the apparent resistivity at the bottom of the #5 dam is in the range of 24–35 Ωm, indicating a substantial increase in the soil water content compared to the top of the dam. In addition, the apparent resistivity of the arable land downstream of the #5 dam varied significantly at different depths and horizontal distances. In terms of depth, unlike the #5 dam, the apparent resistivity gradually decreases from the bottom to the top in the arable land, and the lowest apparent resistivity is only approximately 20 Ωm at the surface, indicating that the surface soil in the area has a high water content. In terms of horizontal distance, the apparent resistivity of the shallow surface layer of arable land decreases as distance from the #5 dam decreases, indicating that the water content of the shallow soil is higher the closer it is to the dam (Figure 12b).

According to UAV photogrammetry, the difference in elevation between the reservoir water level and the surface of the arable land downstream of the #5 dam is as high as 7 m, resulting in a large hydraulic gradient between the upstream and downstream regions. The dams in the GTW were all filled and compacted by loess during the GLCP, and no waterproof material was used at the base of the dam. Therefore, higher hydraulic gradients are prone to cause reservoir water to seep around the dam. This explains the gradual decrease in apparent resistivity from top to bottom in the dam and the gradual increase in apparent resistivity from top to bottom in the arable land downstream of the dam (Figure 12b). In addition, arable land closer to the dam has a higher soil water content and experiences a continuous rise in the groundwater table since the seepage path of the reservoir water is shorter despite the same hydraulic gradient conditions (Figure 12c) [65]. Under the combined effect of high evapotranspiration in the GTW and the rise in the groundwater level caused by dam seepage, the capillary rise of shallow groundwater causes soluble salts of the loess parent material to precipitate and collect on the surface of arable land, which results in severe soil salinization [63]. Soil salinization could make a large amount of new arable land created by the GLCP unusable, thus causing large areas to be abandoned (Figure 5b,c).

5.3. Failure Mode of Silt Dams

A typical failed silt dam was chosen as a case study, and the deformation and failure patterns of the dam were discussed in detail through long-term observations and UAV photogrammetry. Figure 6 shows the deformation and damage characteristics of this typical dam at different time periods. Prior to 7 July 2018, the downstream slope of the dam collapsed, and a large number of cracks were generated at the top of the dam. At this stage, the dam remains relatively intact, with only localized collapse, and the collapsed loess is deposited at the toe of the dam (Figure 6b). Then, from 7–11 July 2018, the accumulated rainfall in the region reached 87.3 mm, with a maximum daily rainfall of 40.3 mm (Figure 13). The continuous rainfall prompted further damage to the silt dam, mainly in the form of collapse along the cracks at the top of the dam, with the collapsed loess sliding along the sloped surface and carrying the accumulated soil from the first collapse downstream to the arable land (Figures 6c and 14a,b). Continued damage also caused dense cracks in the dam top with cumulative displacements of 82.7 mm, increasing the incompleteness of the dam and the potential for reservoir water seepage (Figure 6f). From 7–13 August 2018, continuous rainfall occurred again in the region, with cumulative and maximum daily rainfall of 47.9 mm and 23.8 mm, respectively (Figure 13). The silt dam again underwent progressive deformation driven by rainfall during this period, with the cumulative displacement of the crack gauge reaching 113 mm. Finally, on 21 August 2018, the remaining dam body collapsed completely, the indium wire of the crack gauge broke, and the reservoir water overflowed, as shown in Figure 6d,g.

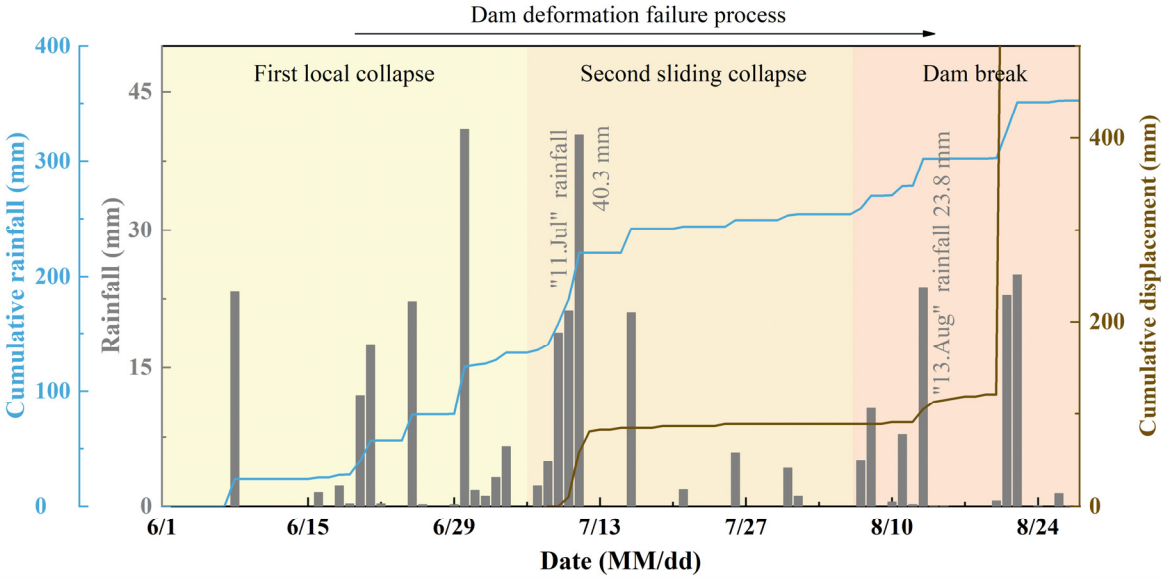

Figure 13. Regional rainfall data and cumulative displacement for typical cases of failed dams in 2018, including the process of dam deformation and failure.

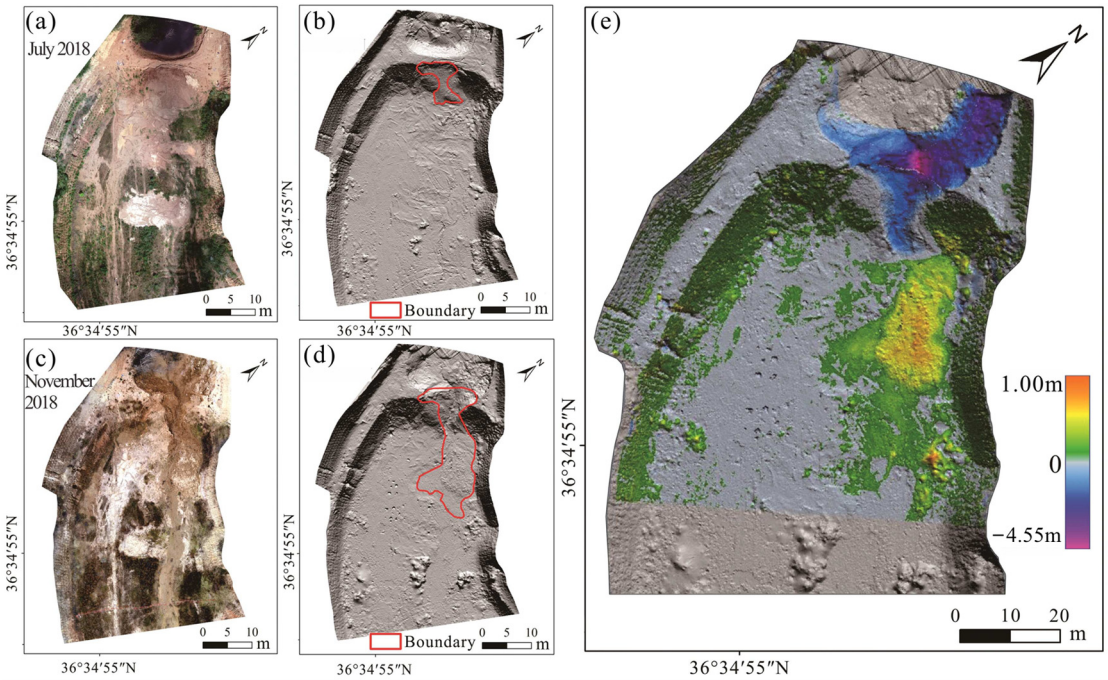

Figure 14. Topographic changes in the selected silt dam. (**a**,**b**) DOM and DEM of the dam on 15 July 2018; (**c**,**d**) DOM and DEM of the dam on 7 November 2018; (**e**) topographic changes in the dam from 15 July 2018, to 7 November 2018. The red polygons in panels (**b**,**d**) highlight the deformed areas of the silt dam.

This deformation process is further revealed by the DEM before and after dam failure, as obtained from UAV photogrammetry (Figures 13d and 14b). The differential results of the two DEMs on 15 July 2018, and 7 November 2018, showed that the maximum break depth and width of the dam reached 4.5 m and 16.9 m, respectively, after the overall failure (Figure 14e). In addition, after the dam failed, the loess of the dam body accumulated in the downstream arable land with maximum and average thicknesses of 1 m and 0.5 m, respectively, and in a shape indicative of fluid-driven deposition.

Because the dam body was not completely compacted during construction, areas of high permeability existed within it. Under the action of high hydraulic gradients caused by reservoir water, seepage channels may be formed in the dam, and then internal erosion may occur, which could significantly reduce the stability of the dam. In addition, the high correlation between dam damage and precipitation indicates that precipitation has an important role in controlling the damage of loess dams. First, under continuous rainfall conditions, the rise in reservoir water level raised the hydraulic gradient and resultant seepage. On the other hand, the infiltration of rainwater along the cracks at the top of the dam further weakened the loess dam, eventually leading to localized sliding of the dam body along the top cracks. Under the long-term osmotic damage and softening effect of reservoir water and rainfall, the dam continuously accrued local sliding damage, which expanded the cracks at the top of the dam, while the width of the dam top gradually decreased or even disappeared (Figure 6). Under this scenario, the reservoir water will be able to break the dam, regardless of ambient rainfall intensity, and will result in an overall dam breach that leaves an approximate "V"-shape in the dam remnants (Figures 13 and 14).

Remote sensing interpretation and field investigations indicate that almost every branch gully in the GTW had a silt dam break in 2020 (Figure 9), which could be attributed to heavy rainfall during the rainy season. Since there is almost no drainage in the silt dam, under the conditions of concentrated heavy rainfall, a large amount of rainwater accumulates in the arable land upstream of the dam and causes the water level to rise. This accumulated rainwater will generate seepage channels within the loess dam and even lead to damage through osmosis. In addition, the dam body undergoes progressive collapse due to long-term immersion and softening by the accumulated rainwater upstream. Under the repeated action of seepage erosion and rainfall softening, the dam eventually breaks. After the dam break, the rainwater accumulated in the upstream arable land will rapidly carry the dam's loess into the downstream arable land, which not only destroys a large number of crops but also further raises the surface water level of the downstream arable land. This process will aggravate downstream dam failure under hydrodynamic action, thus causing a cascade failure of the dams in the gully and increasing the risk and losses of disaster [66].

5.4. Regional Disaster Chain

After the implementation of the GLCP, different types and degrees of geological hazards occurred in the GTW due to the significant changes in the geological environment. A comprehensive analysis by combining multiple methods showed that the soil erosion in the GTW was exacerbated by the excavated slopes since reasonable vegetation restoration measures were not followed during the GLCP. Large-scale gully land consolidation and damming significantly altered the local hydrological cycle, leading to a rise in the groundwater level of arable land and soil salinization. In addition, newly constructed loess silt dams were subjected to osmotic damage and breaching under continuous heavy rainfall conditions. The frequent occurrence of these hazards dramatically limits the economic benefits of the GLCP and poses new and significant challenges to its sustainability on the Loess Plateau.

Interestingly, the different types of disasters in the GTW following the GLCP show a strong spatial correlation (Figure 15a). In other words, multiple hazards are spatially linked within the GTW by surface water flow paths. This results in a hazard chain consisting of slope erosion, silt dam failure, and soil salinization of proximal farmlands downstream of the dam (Figure 15b). Specifically, under heavy rainfall conditions, slope erosion first occurs on a substantial number of steeper slopes excavated during the GLCP in the GTW (Figure 15c). The eroded soil then follows the rainwater downstream along the gully and deposits in the relatively gentle newly created arable land upstream of the silt dam. However, the converged rainwater raises the water level upstream of the silt dam and percolates through the soil downstream, causing osmotic damage and thus causing the dam to breach (Figure 15d). Additionally, this raises the groundwater level in the downstream arable land, which causes soil salinization (Figure 15f). In general, a series of chained geological hazards

occurred in succession after the GLCP was completed in the GTW with the involvement and driving effect of surface water. Therefore, a variety of integrated measures to control the impact of surface water in the GTW are crucial for disaster prevention and control. The construction of water collection cisterns at the peak of the slopes or increasing the vegetation restoration on the slope would help reduce the washing and erosion of rainwater on the slope. In addition, the construction and improvement of drainage channels in gullies and silt dams would enable the timely discharge of the surface water that accumulates upstream, which may prevent dam breaks and reduce the soil salinization caused by rising water levels [67].

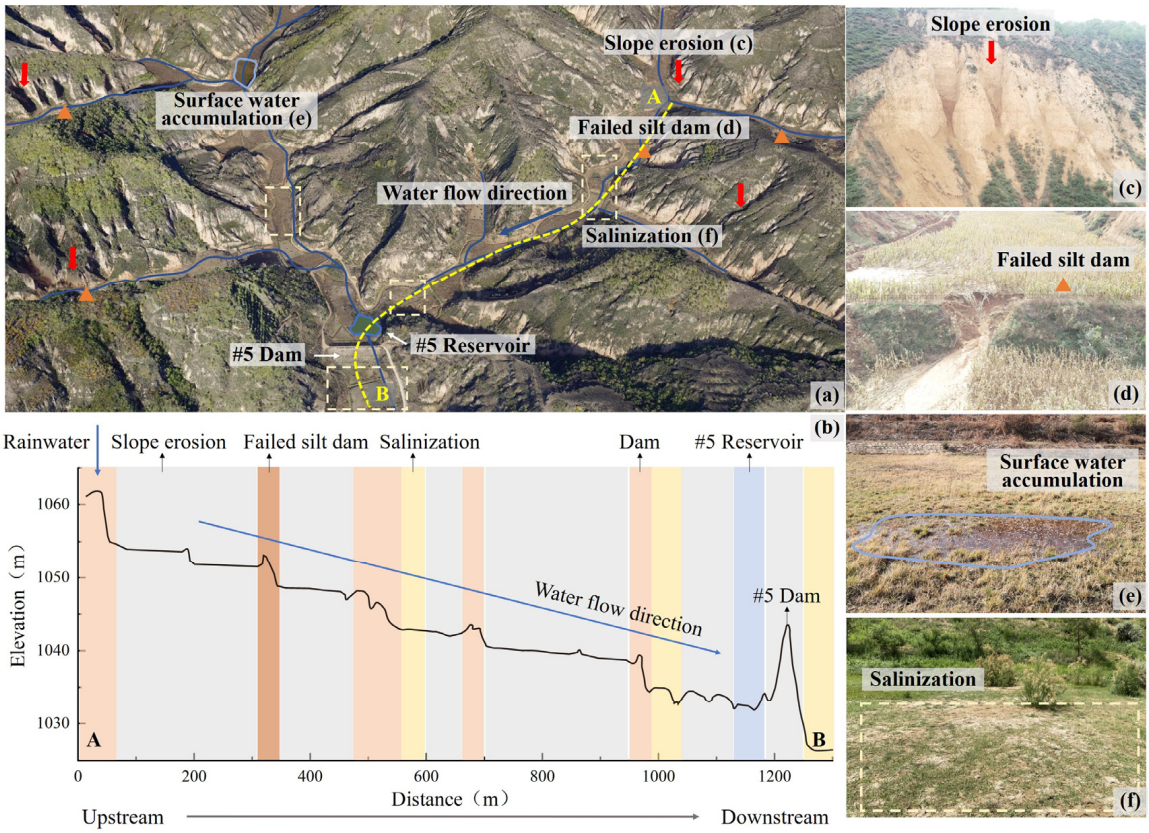

Figure 15. Disaster chain in the GTW and some field photos. (**a**) Spatial distribution of regional disasters; (**b**) spatial distribution of geohazards along the A–B profile; (**c**) site photo of slope erosion; (**d**) site photo of the failed silt dam; (**e**) surface water accumulation on the surface of arable land; (**f**) site photo of saline particles precipitating on the surface of arable land.

6. Conclusions

In this study, a comprehensive investigation and study of the geohazards generated by the implementation of the GLCP in the GTW was conducted through the combination of remote sensing analysis, UAV photogrammetry, geophysical exploration, and field surveys. First, the assessment of soil erosion change characteristics in the GTW by the RUSLE model showed that soil erosion followed an overall increasing trend from 2018 to 2020 after the GLCP was completed, and the localized intensity of soil erosion was significantly correlated with topography and rainfall-related factors. Then, the spatial patterns and mechanisms of salinized arable land were investigated by combining remote sensing analysis and ERT detection. A total of 195 areas containing pronounced salt precipitation were identified in the newly created arable land. This was caused by a combination of external factors, such as a high water table and high evaporation rate. Next, the spatial distribution and failure patterns of silt dam breaks were also examined by remote sensing interpretation and UAV photogrammetry. Up to 20 and 59 silt dams broke in 2018 and 2020 in the GTW,

respectively. Osmosis damage and softening caused by the interaction of the incomplete compaction of the loess dam and concentrated heavy rainfall led to the cascading failure of the gully dam. In addition, strong spatial correlations of the three geohazards detected in the GTW following completion of the GLCP were observed, which resulted in a hazard chain consisting of slope erosion, silt dam failure, and salinization of near-dam farmlands downstream along the surface water flow path. These findings contribute to the decision making needed for hazard mitigation and to the future sustainability of the GLCP. In the near future, in situ monitoring data and remote sensing analysis will be integrated to further understand the hazard patterns and interrelationships to gain comprehensive and in-depth insight into the hazard effects in the GTW following the implementation of the GLCP.

Author Contributions: Conceptualization, X.W. and Q.X.; methodology, X.W.; formal analysis, C.P.; data curation, K.Z.; writing—original draft preparation, X.W.; investigation, Z.L. and W.C.; visualization, D.X. funding acquisition, Q.X.; validation, W.L. All authors have read and agreed to the published version of the manuscript.

Funding: This research was funded by the National Natural Science Foundation of China (Grant No. 41790445, 41630640, 42207200).

Data Availability Statement: The optical remote sensing images utilized in this study can be obtained from Google Earth.

Conflicts of Interest: The authors declare no conflict of interest.

Abbreviations

GLCP, Gully Land Consolidation Project; GTW, Gutun watershed; RUSLE, Revised Universal Soil Loss Equation; ERT, electrical resistivity tomography; UAV, unmanned aerial vehicle; USLE, Universal Soil Loss Equation; SSD, Soil Science Database; DOM, digital orthophoto map; DEM, digital elevation model; EPIC, Erosion-Productivity Impact Calculator; CSLE, Chinese Soil Loss Equation; GWL, groundwater level; GW, groundwater.

References

1. Derbyshire, E. Geological hazards in loess terrain, with particular reference to the loess regions of China. *Earth-Sci. Rev.* **2001**, *54*, 231–260. [CrossRef]
2. Xu, L.; Dai, F.C.; Tu, X.B.; Javed, I.; Woodard, M.J.; Jin, Y.L.; Tham, L.G. Occurrence of landsliding on slopes where flowsliding had previously occurred: An investigation in a loess platform, North-west China. *Catena* **2013**, *104*, 195–209. [CrossRef]
3. Bryan, B.A.; Gao, L.; Ye, Y.; Sun, X.; Connor, J.D.; Crossman, N.D.; Stafford-Smith, M.; Wu, J.; He, C.; Yu, D.; et al. China's response to a national land-system sustainability emergency. *Nature* **2018**, *559*, 193–204. [CrossRef] [PubMed]
4. Fu, B. Soil erosion and its control in the loess plateau of China. *Soil Use Manag.* **1989**, *5*, 76–82. [CrossRef]
5. Liu, Q.; Zhi, L. A Review of Compensation in Convertion of Farmland to Forest Program. *World For. Res.* **2010**, *23*, 45–49.
6. Liu, Z.P.; Shao, M.A.; Wang, Y.Q. Large-scale spatial interpolation of soil pH across the Loess Plateau, China. *Environ. Earth Sci.* **2013**, *69*, 2731–2741. [CrossRef]
7. Tang, K.; Zhang, K.; Lei, A. Critical slope gradient for compulsory abandonment of farmland on the hilly Loess Plateau. *Chin. Sci. Bull.* **1998**, *43*, 409–412. [CrossRef]
8. Lü, Y.; Fu, B.; Feng, X.; Zeng, Y.; Liu, Y.; Chang, R.; Sun, G.; Wu, B. A policy-driven large scale ecological restoration: Quantifying ecosystem services changes in the loess plateau of China. *PLoS ONE* **2012**, *7*, e31782. [CrossRef]
9. Chen, Y.; Wang, K.; Lin, Y.; Shi, W.; Song, Y.; He, X. Balancing green and grain trade. *Nat. Geosci.* **2015**, *8*, 739–741. [CrossRef]
10. Lei, N.; Mu, X.M. Analysis on effect of gully control and land reclamation projects on carbon emission in hilly and gully regions of Loess Plateau. *J. Agro-Environ. Sci.* **2018**, *37*, 392–398. [CrossRef]
11. Yurui, L.; Yi, L.; Pengcan, F.; Hualou, L. Impacts of land consolidation on rural human–environment system in typical watershed of the Loess Plateau and implications for rural development policy. *Land Use Policy* **2019**, *86*, 339–350. [CrossRef]
12. Jin, Z.; Guo, L.; Wang, Y.; Yu, Y.; Lin, H.; Chen, Y.; Chu, G.; Zhang, J.; Zhang, N. Valley reshaping and damming induce water table rise and soil salinization on the Chinese Loess Plateau. *Geoderma* **2019**, *339*, 115–125. [CrossRef]
13. Liu, Q.; Wang, Y.; Zhang, J.; Chen, Y. Filling gullies to create farmland on the Loess Plateau. *Environ. Sci. Technol.* **2013**, *47*, 7589–7590. [CrossRef]
14. Li, Y.; Du, G.; Liu, Y. Transforming the Loess Plateau of China. *Front. Agric. Sci. Eng.* **2016**, *3*, 181–185. [CrossRef]

15. Pu, C.; Xu, Q.; Zhao, K.; Jiang, Y.; Hao, L.; Liu, J.; Chen, W.; Kou, P. Characterizing the topographic changes and land subsidence associated with the mountain excavation and city construction on the Chinese loess plateau. *Remote Sens.* **2021**, *13*, 1556. [CrossRef]
16. Wang, X.; Xu, Q.; Zhao, K.; Ye, Z.; Guo, P.; Guo, C. Distribution Rule of Govening Valleys Project in Baota District of Yan'an City. *Bull. Soil Water Conserv.* **2019**, *39*, 141–148.
17. He, C. How to develop modern agriculture in Yan'an. *J. Yanan Univ. Social Sci.* **2013**, *35*, 62–65.
18. Jin, Z. The creation of farmland by gully filling on the Loess Plateau: A double-edged sword. *Environ. Sci. Technol.* **2014**, *48*, 883–884. [CrossRef]
19. Börjesson, P.; Tufvesson, L.M. Agricultural crop-based biofuels—Resource efficiency and environmental performance including direct land use changes. *J. Clean. Prod.* **2011**, *19*, 108–120. [CrossRef]
20. Juang, C.H.; Dijkstra, T.; Wasowski, J.; Meng, X. Loess geohazards research in China: Advances and challenges for mega engineering projects. *Eng. Geol.* **2019**, *251*, 1–10. [CrossRef]
21. Zhao, Y.; Wang, Y.; Wang, L.; Zhang, X.; Yu, Y.; Jin, Z.; Lin, H.; Chen, Y.; Zhou, W.; An, Z. Exploring the role of land restoration in the spatial patterns of deep soil water at watershed scales. *Catena* **2019**, *172*, 387–396. [CrossRef]
22. Xu, Q.; Chen, W.; Zhao, K.; Zhou, X.; Du, P.; Guo, C.; Ju, Y.; Pu, C. Effects of land-use management on soil erosion: A case study in a typical watershed of the hilly and gully region on the Loess Plateau of China. *Catena* **2021**, *206*, 105551. [CrossRef]
23. Chen, W.; Xu, Q.; Zhao, K.; Zhou, X.; Li, S.; Wang, J.; Wang, X.; Xu, J. Spatial analysis of land-use management for gully land consolidation on the Loess Plateau in China. *Ecol. Indic.* **2020**, *117*, 106633. [CrossRef]
24. Lacroix, P.; Dehecq, A.; Taipe, E. Irrigation-triggered landslides in a Peruvian desert caused by modern intensive farming. *Nat. Geosci.* **2020**, *13*, 56–60. [CrossRef]
25. Karydas, C.G.; Panagos, P.; Gitas, I.Z. A classification of water erosion models according to their geospatial characteristics. *Int. J. Digit. Earth* **2014**, *7*, 229–250. [CrossRef]
26. George, K.J.; Kumar, S.; Hole, R.M. Geospatial modelling of soil erosion and risk assessment in Indian Himalayan region—A study of Uttarakhand state. *Environ. Adv.* **2021**, *4*, 100039. [CrossRef]
27. Galdino, S.; Sano, E.E.; Andrade, R.G.; Grego, C.R.; Nogueira, S.F.; Bragantini, C.; Flosi, A.H.G. Large-scale Modeling of Soil Erosion with RUSLE for Conservationist Planning of Degraded Cultivated Brazilian Pastures. *Land Degrad. Dev.* **2016**, *27*, 773–784. [CrossRef]
28. Benavidez, R.; Bethanna, J.; Deborah, M.; Kevin, N. A-review-of-the-Revised-Universal-Soil-Loss-Equation-RUSLE-With-a-view-to-increasing-its-global-applicability-and-improving-soil-loss-estimates. *Hydrol. Earth Syst. Sci.* **2018**, *22*, 6059–6086. [CrossRef]
29. Borrelli, P.; Robinson, D.A.; Fleischer, L.R.; Lugato, E.; Ballabio, C.; Alewell, C.; Meusburger, K.; Modugno, S.; Schütt, B.; Ferro, V.; et al. An assessment of the global impact of 21st century land use change on soil erosion. *Nat. Commun.* **2017**, *8*, 2013. [CrossRef]
30. Alewell, C.; Borrelli, P.; Meusburger, K.; Panagos, P. Using the USLE: Chances, challenges and limitations of soil erosion modelling. *Int. Soil Water Conserv. Res.* **2019**, *7*, 203–225. [CrossRef]
31. Yan, R.; Zhang, X.; Yan, S.; Chen, H. Estimating soil erosion response to land use/cover change in a catchment of the Loess Plateau, China. *Int. Soil Water Conserv. Res.* **2018**, *6*, 13–22. [CrossRef]
32. Zhao, G.; Kondolf, G.M.; Mu, X.; Han, M.; He, Z.; Rubin, Z.; Wang, F.; Gao, P.; Sun, W. Sediment yield reduction associated with land use changes and check dams in a catchment of the Loess Plateau, China. *Catena* **2017**, *148*, 126–137. [CrossRef]
33. Sun, W.; Shao, Q.; Liu, J. Soil erosion and its response to the changes of precipitation and vegetation cover on the Loess Plateau. *J. Geogr. Sci.* **2013**, *23*, 1091–1106. [CrossRef]
34. Wang, J.; Lu, P.; Valente, D.; Petrosillo, I.; Babu, S.; Xu, S.; Li, C.; Huang, D.; Liu, M. Analysis of soil erosion characteristics in small watershed of the loess tableland Plateau of China. *Ecol. Indic.* **2022**, *137*, 108765. [CrossRef]
35. Liu, Y.; Guo, Y.; Li, Y.; Li, Y. GIS-based effect assessment of soil erosion before and after gully land consolidation: A case study of Wangjiagou project region, Loess Plateau. *Chinese Geogr. Sci.* **2015**, *25*, 137–146. [CrossRef]
36. Han, X.; Lv, P.; Zhao, S.; Sun, Y.; Yan, S.; Wang, M.; Han, X.; Wang, X. The Effect of the Gully Land Consolidation Project on soil erosion and crop production on a typical Watershed in the Loess Plateau. *Land* **2018**, *7*, 113. [CrossRef]
37. Guo, Z.; Gao, J.; Sun, P.; Dou, S.; Li, J.; Lou, X.; Wang, H.; Ahmad, R.; Gao, Z. Influence of Gully Land Consolidation on Phreatic Water Transformation in the Loess Hilly and Gully Region. *Water* **2021**, *13*, 538. [CrossRef]
38. Xu, J.; Wei, W.; Bao, H.; Zhang, K.; Lan, H.; Yan, C.; Sun, W. Failure models of a loess stacked dam: A case study in the Ansai Area (China). *Bull. Eng. Geol. Environ.* **2020**, *79*, 1009–1021. [CrossRef]
39. Zhao, M.; Liu, P.; Jiang, L.; Wang, K. The influence of internal erosion in earthen dams on the potential difference response to applied voltage. *Water* **2021**, *13*, 3387. [CrossRef]
40. Ning, T.; Li, Z.; Liu, W.; Han, X. Evolution of potential evapotranspiration in the northern Loess Plateau of China: Recent trends and climatic drivers. *Int. J. Climatol.* **2016**, *36*, 4019–4028. [CrossRef]
41. Cortina, J.; Amat, B.; Castillo, V.; Fuentes, D.; Maestre, F.T.; Padilla, F.M.; Rojo, L. The restoration of vegetation cover in the semi-arid Iberian southeast. *J. Arid Environ.* **2011**, *75*, 1377–1384. [CrossRef]
42. Huang, J.; Zhang, W.; Zuo, J.; Bi, J.; Shi, J.; Wang, X.; Chang, Z.; Huang, Z.; Yang, S.; Zhang, B.; et al. An overview of the semi-arid climate and environment research observatory over the loess plateau. *Adv. Atmos. Sci.* **2008**, *25*, 906–921. [CrossRef]

43. Liu, Y.; Chen, Z.; Li, Y.; Feng, W.; Cao, Z. The Planting Technology and Industrial Development Prospects of Forage Rape in the Loess Hilly Area—A Case Study of Newly-increased Cultivated Land Through Gully Land Consolidation in Yan'an, Shaanxi Province. *J. Nat. Resour.* **2017**, *32*, 2065–2074.
44. Elnashar, A.; Zeng, H.; Wu, B.; Fenta, A.A.; Nabil, M.; Duerler, R. Soil erosion assessment in the Blue Nile Basin driven by a novel RUSLE-GEE framework. *Sci. Total Environ.* **2021**, *793*, 148466. [CrossRef]
45. Getnet, T.; Mulu, A. Assessment of soil erosion rate and hotspot areas using RUSLE and multi-criteria evaluation technique at Jedeb watershed, Upper Blue Nile, Amhara Region, Ethiopia. *Environ. Chall.* **2021**, *4*, 100174. [CrossRef]
46. Abbaszadeh Shahri, A.; Spross, J.; Johansson, F.; Larsson, S. Landslide susceptibility hazard map in southwest Sweden using artificial neural network. *Catena* **2019**, *183*, 104225. [CrossRef]
47. Richardson, C.W.; Foster, G.R.; Wright, D.A. Estimation of erosion index from daily rainfall amount. *Trans. Am. Soc. Agric. Eng.* **1983**, *26*, 153–156. [CrossRef]
48. Zhang, W.B.; Fu, J.S. Rainfall Erosivity Estimation Under Different Rainfall Amount. *Resour. Sci.* **2003**, *25*, 35–41.
49. Panagos, P.; Borrelli, P.; Meusburger, K.; Yu, B.; Klik, A.; Lim, K.J.; Yang, J.E.; Ni, J.; Miao, C.; Chattopadhyay, N.; et al. Global rainfall erosivity assessment based on high-temporal resolution rainfall records. *Sci. Rep.* **2017**, *7*, 4175. [CrossRef]
50. Williams, J.R.; Renard, K.G.; Dyke, P.T. EPIC: A new method for assessing erosion's effect on soil productivity. *J. Soil Water Conserv.* **1983**, *38*, 381–383.
51. Ghaderi, A.; Abbaszadeh Shahri, A.; Larsson, S. A visualized hybrid intelligent model to delineate Swedish fine-grained soil layers using clay sensitivity. *Catena* **2022**, *214*, 106289. [CrossRef]
52. Fu, S.; Liu, B. Evolution of the Soil Erosion Model. *Adv. Earth Sci.* **2002**, *17*, 78–84. [CrossRef]
53. Liu, B.Y.; Nearing, M.A.; Risse, L.M. Slope gradient effects on soil loss for steep slopes. *Trans. Am. Soc. Agric. Eng.* **1994**, *37*, 1835–1840. [CrossRef]
54. McCool, D.K.; Brown, L.C.; Foster, G.R.; Mutchler, C.K.; Meyer, L.D. Revised Slope Steepness Factor for the Universal Soil Loss Equation. *Trans. Am. Soc. Agric. Eng.* **1987**, *30*, 1387–1396. [CrossRef]
55. Sun, W.; Shao, Q.; Liu, J.; Zhai, J. Assessing the effects of land use and topography on soil erosion on the Loess Plateau in China. *Catena* **2014**, *121*, 151–163. [CrossRef]
56. Li, Y.; Xie, Z.; Qin, Y.; Sun, Y. Temporal-spatial variation characteristics of soil erosion in the pisha sandstone area, loess plateau, china. *Pol. J. Environ. Stud.* **2019**, *28*, 2205–2214. [CrossRef]
57. Wischmeier, W.H.; Smith, D.D. Rainfall Energy and Its Relationship to Soil Loss. *Eos Trans. Am. Geophys. Union* **1958**, *39*, 285–291. [CrossRef]
58. Peng, D.; Xu, Q.; Zhang, X.; Xing, H.; Zhang, S.; Kang, K.; Qi, X.; Ju, Y.; Zhao, K. Hydrological response of loess slopes with reference to widespread landslide events in the Heifangtai terrace, NW China. *J. Asian Earth Sci.* **2019**, *171*, 259–276. [CrossRef]
59. Bian, S.; Chen, G.; Zeng, R.; Meng, X.; Jin, J.; Lin, L.; Zhang, Y.; Shi, W. Post-failure evolution analysis of an irrigation-induced loess landslide using multiple remote sensing approaches integrated with time-lapse ERT imaging: Lessons from Heifangtai, China. *Landslides* **2022**, *19*, 1179–1197. [CrossRef]
60. Zeng, R.Q.; Meng, X.M.; Zhang, F.Y.; Wang, S.Y.; Cui, Z.J.; Zhang, M.S.; Zhang, Y.; Chen, G. Characterizing hydrological processes on loess slopes using electrical resistivity tomography—A case study of the Heifangtai Terrace, Northwest China. *J. Hydrol.* **2016**, *541*, 742–753. [CrossRef]
61. Zou, X. Study on the Influence of Groundwater Level Raising on the Salt Distribution of Surface Loess: A Case Study in Heifangtai and Gutun. Master's Thesis, Chengdu University of Technology, Chengdu, China, 2020.
62. Wang, Y.; Chen, L.; Gao, Y.; Wang, S.; Lü, Y.; Fu, B. Carbon Sequestration Function of Check-Dams: A Case Study of the Loess Plateau in China. *Ambio* **2014**, *43*, 926–931. [CrossRef] [PubMed]
63. Singh, A. Soil salinization and waterlogging: A threat to environment and agricultural sustainability. *Ecol. Indic.* **2015**, *57*, 128–130. [CrossRef]
64. Singh, A. Groundwater modelling for the assessment of water management alternatives. *J. Hydrol.* **2013**, *481*, 220–229. [CrossRef]
65. Li, H. Study on Farmland Salinization and Its Mechanism in the Loess Plateau. Ph.D. Thesis, Tottori University, Tottori, Japan, 2012; pp. 95–102.
66. Cao, Z.; Yue, Z.; Pender, G. Flood hydraulics due to cascade landslide dam failure. *J. Flood Risk Manag.* **2011**, *4*, 104–114. [CrossRef]
67. Fan, X.; Pedroli, B.; Liu, G.; Liu, Q.; Liu, H.; Shu, L. Soil salinity development in the yellow river delta in relation to groundwater dynamics. *L. Degrad. Dev.* **2012**, *23*, 175–189. [CrossRef]